

Mathematical analysis of mural thrombogenesis

Concentration profiles of platelet-activating agents and effects of viscous shear flow

Bernard J. Folie and Larry V. McIntire

Department of Chemical Engineering (Biomedical Engineering Laboratory), Rice University, Houston, Texas 77251

ABSTRACT The concentration profiles of adenosine diphosphate (ADP), thromboxane A₂ (TxA₂), thrombin, and von Willebrand factor (vWF) released extracellularly from the platelet granules or produced metabolically on the platelet membrane during thrombus growth, were estimated using finite element simulation of blood flow over model thrombi of various shapes and dimensions. The wall fluxes of these platelet-activating agents were estimated for each model thrombus at three different wall shear rates (100 s⁻¹, 800 s⁻¹, and 1,500 s⁻¹), employing experimental data on thrombus growth rates and sizes. For that purpose, whole human blood was perfused in a parallel-plate flow chamber coated with type I fibrillar human collagen, and the kinetic data collected and analyzed by an EPI-fluorescence video microscopy system and a digital image processor. It was found that thrombin concentrations were large enough to cause irreversible platelet aggregation.

Although heparin significantly accelerated thrombin inhibition by antithrombin III, the remaining thrombin levels were still significantly above the minimum threshold required for irreversible platelet aggregation. While ADP concentrations were large enough to cause irreversible platelet aggregation at low shear rates and for small aggregate sizes, TxA₂ concentrations were only sufficient to induce platelet shape change over the entire range of wall shear rates and thrombi dimensions studied. Our results also indicated that the local concentration of vWF multimers released from the platelet α -granules could be sufficient to modulate platelet aggregation at low and intermediate wall shear rates (<1,000 s⁻¹).

The sizes of standing vortices formed adjacent to a growing aggregate and the embolizing stresses and the torque, acting at the aggregate surface, were also estimated in this simulation. It was found that standing vortices developed on both sides of the

thrombus even at low wall shear rates. Their sizes increased with thrombus size and wall shear rate, and were largely dependent upon thrombus geometry. The experimental observation that platelet aggregation occurred predominantly in the spaces between adjacent thrombi, confirmed the numerical prediction that those standing vortices are regions of reduced fluid velocities and high concentrations of platelet-activating substances, capable of trapping and stimulating platelets for aggregation. The average shear stress and normal stress, as well as the torque, acting to detach the thrombus, increased with increasing wall shear rate. Both stresses were found to be nearly independent of thrombus size and only weakly dependent upon thrombus geometry. Although both stresses had similar values at low wall shear rates, the average shear stress became the predominant embolizing stress at high wall shear rates.

INTRODUCTION

Blood platelets have been recognized as major contributors to the normal hemostatic mechanism as well as its derived pathological state, thrombosis, for decades (1, 2). Indeed, when blood platelets flow near the subendothelium of an injured blood vessel (3, 4), an artificial polymeric surface used in a prosthetic blood-contacting device (5), or an atherosclerotic lesion (6), a number of hemorheological and biochemical events take place very rapidly near that site to form thrombi (solid platelet aggregates) on the reactive surface. Clinically, the com-

plications of thrombosis occur as local obstruction of blood vessels or distal embolization of the thrombus, interrupting blood flow downstream, thereby limiting oxygen transport to tissues, leading to ischemia or infarction (6).

Following initial platelet adhesion and activation on the reactive surface, biochemical proaggregatory agents are released extracellularly from the platelet granules or produced metabolically on the platelet membrane. Accumulating in high concentration locally at the site of aggregate formation, these platelet-activating substances act synergistically to activate additional platelets and accelerate the process of thrombus growth (7). Releasable materials are important in normal thrombogenesis, for platelets lacking these agents (storage pool disease),

Address reprint requests to Dr. Larry V. McIntire, Department of Chemical Engineering, Rice University, P.O. Box 1892, Houston, TX 77251.

have been shown to have reduced thrombus formation on subendothelium and fibrillar collagen (8).

Because the relative importance of most proaggregatory substances in inducing mural thrombogenesis is still uncertain, and because direct measurement of very low concentrations of chemicals in a dynamic system is difficult, a two-dimensional theoretical model, involving the simulation of blood flow between two parallel plates over a model thrombus attached to the bottom plate, was developed. Four potential platelet-activating agents were investigated. Adenosine diphosphate (ADP) and von Willebrand factor (vWF) are released, respectively, from the dense and α -granules of activated platelets, while thromboxane A_2 (Tx A_2) and thrombin are enzymatically generated on or near the platelet membrane (9). For each agent, the estimated maximum concentration in the neighborhood of one thrombus or two adjacent thrombi generating and releasing that compound, was compared with the concentration known to affect platelet function in various *in vitro* measurement systems.

Because the local concentration profiles of releasable substances depend primarily on the rate of thrombus growth or the thrombus size, and on the rate of transport of those substances from the aggregate site, concentration profiles were computed as a function of wall shear rate. This is the main fluid mechanical variable controlling surface access. Indeed, blood flow greatly increases the effective diffusivity of cells and proteins, through a red blood cell (RBC) rotation and/or an interparticle collision mechanism, in a shear rate dependent manner (10). Because the thrombogenesis process occurs near the surface where the local concentration of RBCs is low, the increased diffusivity is predominantly due to the rotation of RBCs in a shear field, and Keller's mixing model (11, 12) was used to estimate the enhanced diffusivities of platelet-activating agents in whole blood.

An EPI-fluorescence video microscopy system, coupled with digital image processing techniques, was utilized to determine experimentally the rates of growth and sizes of individual thrombi at different wall shear rates, ranging from 100 s^{-1} (a typical venous shear rate) to $1,500 \text{ s}^{-1}$ (an arterial shear rate). Whole human blood was perfused in a parallel-plate flow chamber coated with human collagen type I fibrils, a predominant thrombogenic protein found in the subendothelium of injured blood vessels (13). The data obtained in those experiments were then used in the mathematical model to estimate the wall fluxes of platelet-activating agents at various wall shear rates.

Only two papers using similar microscopic modelling have been reported in the literature. The first one used only a qualitative approach to determine the approximate shapes of the concentration contours generated (14). The second one, from our laboratory, did investigate the role of several platelet-activating substances in promoting

thrombus growth, but using a one-dimensional model of a flat thrombus, and ignoring the presence of RBCs (15). Consequently, neither the flow disturbances caused by the finite size of the growing platelet aggregates nor the effect of shear rate on the magnitude of the wall flux of platelet-activating agents were considered.

The purpose of the present paper is, therefore, to estimate computationally the concentration profiles of four proaggregatory compounds (ADP, Tx A_2 , thrombin, vWF) released from a more realistic model thrombus, thereby gaining some insight into which platelet-activating substances affect the mechanism of thrombus growth on a microscopic scale. The effect of flow, aggregate size, aggregate geometry, and number of aggregates on those concentration profiles was also investigated. Finally, while some effects of disturbed flow and vortices in thrombogenesis have been measured experimentally by others (16, 17), the size of the recirculating regions developing on both sides of a thrombus, as well as the magnitude of the embolizing stresses and the torque, acting at the thrombus surface, were estimated in the simulation, and their physiological relevance discussed.

MATERIALS AND METHODS

Collagen preparation

2.5 mg of type I acid-soluble human collagen (Sigma Chemical Co., St. Louis, MO) purified by a pepsin extraction and salt fractionation method from human placenta (18) were mixed with 1 ml of 0.012 N HCl (pH 2) cooled at 4°C in a polypropylene test tube. The test tube was then placed on a low-speed nutator and the collagen allowed to dissolve completely for one h at ambient temperature. This monomeric collagen (tropocollagen) solution was kept at 4°C until further utilization. A neutralized, isotonic collagen solution was then prepared by mixing 1 ml of chilled tropocollagen solution with $104.2 \mu\text{l}$ of 0.1 M NaOH and $104.2 \mu\text{l}$ of 10 X phosphate-buffered saline solution (0.2 M Na_2HPO_4 , 1.3 M NaCl, pH 7.4) to make a final collagen concentration of 2.07 mg/ml. The pH of that solution was adjusted to 7.4 ± 0.2 by addition of a few drops of 0.01 M HCl or 0.01 M NaOH.

Flow chamber and collagen coating

Heparin-anticoagulated whole blood with fluorescent-labelled platelets, prepared as previously reported (19), was aspirated by a syringe pump (Harvard Apparatus Co., Inc., South Natick, MA, Model 935) for two and a half minutes at a controlled shear rate of 100 s^{-1} , 800 s^{-1} , or $1,500 \text{ s}^{-1}$ from a test tube into a polycarbonate parallel-plate flow chamber, described in detail elsewhere.²⁰

The flow chamber, with a final slit width of $205 \mu\text{m}$, served as a model of a small blood vessel with a well-defined fluid-dynamical and rheological environment, suitable for precise analysis of mural thrombogenesis. Before being assembled as part of the flow chamber, 7.4 cm^2 of a glass cover slip (Corning Glass Works, Corning, NY; No. 1, $24 \times 50 \text{ mm}$) were coated with $71.5 \mu\text{l}$ of the neutralized tropocollagen solution (2.07 mg/ml), the remaining portion of the slide being covered with parafilm. The slide was then placed in the bottom of a petri dish (Becton

Dickinson Labware, Oxnard, CA; Falcon 1001, 100 × 15 mm) and collagen fibrillogenesis initiated by allowing the dish to float for 12 min in a water bath preheated at 37°C. This technique, as reported by others (21, 22), allows the monomeric collagen solution to polymerize into native-type collagen fibrils of 67 nm periodicity, shown as the optimum molecular configuration for platelet aggregation (22). The glass cover slip was then placed under a ventilated hood and the collagen gel supernatant allowed to evaporate completely for 30–60 min. The collagen-coated glass was kept in a humid petri dish to prevent the protein from denaturing until assembling of the flow chamber. By this method, the glass cover slip is coated with a continuous layer of type I (by classification) human collagen in fibrillar form, with an average collagen density of ~20 μg/cm², which is within the range of densities required for maximum platelet aggregation (23).

Video microscopy equipment

The parallel plate flow chamber, maintained at 37°C by a thermostatic air bath, was mounted on an inverted-stage microscope (DIAPHOT-TMD, Nikon Inc., Garden City, NY) equipped with an epi-fluorescent illumination attachment, a 100 × oil immersion objective, and a silicon intensified target (SIT) camera (model C-1012, Hamamatsu Corp., Waltham, MA) suitable for very low light levels. The microscopy was performed in EPI or incident-light mode due to the opacity of whole blood. The experiments were recorded real-time on a half-inch color video cassette recorder and the video tapes further analyzed by a digital image processor (Perceptive Systems, Houston, TX; model 327). A more detailed description of the video equipment is available elsewhere (20).

Microscopic data analysis

Digital image processing was used to analyze the kinetics of thrombus growth, to infer the three-dimensional structure of thrombi, and to obtain different morphological information on each thrombus, including basal area and average height at each shear rate. These data were then used in the calculations of fluxes of platelet-activating substances in the mathematical model (see Appendix C). The local visualization of mural thrombogenesis was performed at the location of maximum macroscopic platelet accumulation on the collagen-coated surface, as determined by a microphotometric measurement system, described previously (19). At the low wall shear rates of 100 s⁻¹ and 800 s⁻¹, maximum platelet density occurred near the beginning of the collagen coating because of platelet diffusion-limited processes downstream. At the high wall shear rate of 1,500 s⁻¹ the maximum occurred further downstream because of embolization by fluid drag forces of the larger thrombi formed at the inlet (24). Video tapes of experiments were digitized every 15 s and the digitized images further processed and analyzed using various enhancement and feature extraction routines. Image enhancement was performed by a series of geometric and arithmetic operations, including background subtraction, grey scale linear stretching, and spatial filtering to eliminate the noise and increase object contrast in the original digitized images. Different feature extraction routines were then applied to the processed images to identify the platelets or the thrombi by tracing their perimeters and performing computations on each object.

THEORY

Consider whole blood flowing at low Reynolds number between the two parallel plates of a rectangular channel

200 μm-thick, over a two-dimensional model thrombus attached to the bottom plate. The fluid approaches the thrombus as a Newtonian fully-developed laminar flow with a typical parabolic profile. A species of interest *A* is released from the thrombus surface at a constant specified flux, N_A . Some of the species analyzed will also react by a first order bulk phase reaction, $A \rightarrow B$, where *B* is some inactive form of *A*. The physical situation is depicted in Fig. 1. The different cases treated in this simulation, including the various object geometries and sizes, as well as the situation where two aggregates, located near or far away from each other, are growing on the same surface, are shown in Fig. 2.

Chemical reactions

Thrombin is generated enzymatically on the surface of the platelet, where factor X_a , activated by both the intrinsic and extrinsic pathways, factor V_a , and Ca^{2+} combine with platelet membrane phospholipids to form the prothrombinase complex. This complex can rapidly convert circulating prothrombin to thrombin (9). Because this membrane reaction goes to completion immediately, the rate of release of thrombin from the thrombus surface was assumed equal to the rate of arrival of prothrombin to the thrombus surface. Here we assumed that the amount of thrombin produced from prothrombin diffusing inside the thrombus is small compared with the amount produced on the thrombus surface. Thrombin released is inactivated in the bulk phase by the circulating inhibitor antithrombin III (AT III). This reaction is greatly accelerated in the presence of heparin, a commonly-used antithrombotic agent (25). Mathematically, the reactions

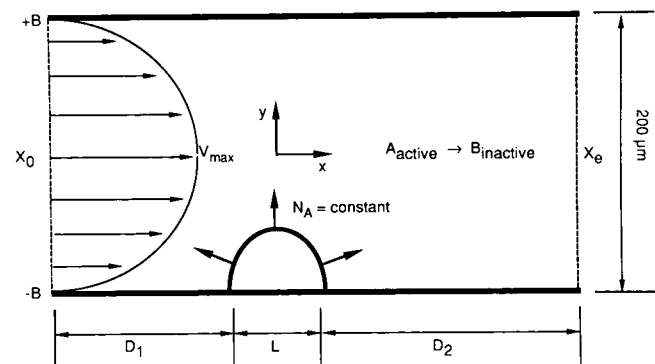


FIGURE 1 Geometry of the parallel-plate flow chamber, used both for the experiments and in the computer simulation. Blood flows from left to right over a semicircular model thrombus of diameter L . A substance *A* is released from the thrombus surface at a constant flux N_A , and then, may become inactivated by a first order chemical reaction in the bulk. The fluid enters as a Newtonian fully developed laminar flow with a typical parabolic profile.

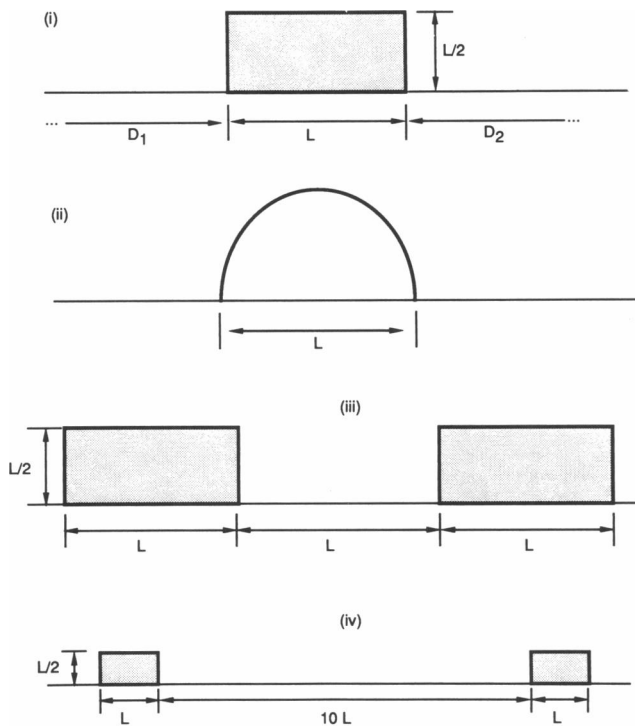
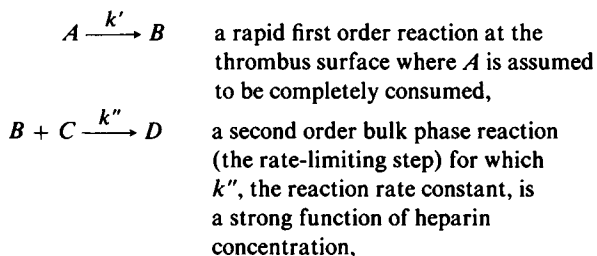


FIGURE 2 Model thrombus sizes and geometries. The six following cases were analyzed: (i) rectangular model thrombus: (a) $L = 10 \mu\text{m}$, $D_1 = 4L$, $D_2 = 10L$; (b) $L = 20 \mu\text{m}$, $D_1 = 4L$, $D_2 = 6L$; (ii) semicircular model thrombus: (a) $L = 10 \mu\text{m}$, $D_1 = 4L$, $D_2 = 10L$; (b) $L = 20 \mu\text{m}$, $D_1 = 4L$, $D_2 = 6L$; (iii) two rectangular thrombi: $L = 20 \mu\text{m}$, $D_1 = 1L$, $D_2 = 6L$; (iv) two rectangular thrombi: $L = 20 \mu\text{m}$, $D_1 = 1L$, $D_2 = 4L$.

can be written as:



where A = prothrombin; B = thrombin; C = AT III; D = inactive complex.

Thromboxane A_2 , an arachidonic acid metabolite, has a short half-life (43 s) in aqueous media and undergoes rapid nonenzymatic hydrolysis to thromboxane B_2 , which is inactive biologically (26). This reaction is as follows:



where $E = \text{Tx}A_2$; $F = \text{Tx}B_2$.

Because ADP and vWF ($\text{ADP} = G$; $\text{vWF} = H$) have

relatively long half-lives, compared with the time required to activate platelets, they were assumed not to react in the bulk phase. Indeed, although ADP is eventually metabolized to AMP by the ADP-ases, studies have indicated half-lives of the order of 20–45 min for ADP in plasma (27). Similarly, studies with plasma vWF have revealed half-lives of several hours for that protein (28). Disappearance of vWF by binding to platelet membrane glycoproteins was also not considered in this study.

Equations

The equations for the steady-state boundary-value problem describing the physical situation shown in Fig. 1 are given in detail in Appendix A. In brief, the equation of motion for an incompressible Newtonian fluid with constant physical properties (the Navier-Stokes equation) and the continuity equation were first solved for the velocity field within the channel. That velocity field was then used to solve the convection-diffusion equation for the concentration profile of each platelet-activating agent developing in the vicinity of a given model thrombus at a specific wall shear rate. Those equations were solved numerically using a finite element method, as explained in depth in Appendix B.

Biodynamical properties

The sizes of the standing vortices developing upstream and downstream of the model thrombi because of the disturbed flow, were estimated by calculating the distribution of the shear stress τ_t , the tangential component of the stress vector, along the bottom plate and the thrombus surface. The i -component of the stress vector \mathbf{t} is given by:

$$\mathbf{t}_i = \sigma_{ij}n_j; \sigma_{ij} = -P\delta_{ij} + \mu(V_{ij} + V_{ji}), \quad (1)$$

where σ_{ij} is the stress tensor; n_j is the unit normal vector at the boundary; and δ_{ij} is the Kronecker delta. Here the comma represents partial differentiation with respect to the following index, and repeated indices imply summation. The separation and reattachment points, as shown in Fig. 3, are defined as the points where the shear stress changes sign. The size of those recirculating regions was also estimated graphically by plotting streamlines around the object. For two-dimensional incompressible flow, the stream function Ψ is the remaining non-zero component of a vector potential which satisfies the continuity equation identically. Therefore, by definition:

$$V_x = \frac{\partial \Psi}{\partial y}; V_y = -\frac{\partial \Psi}{\partial x}. \quad (2)$$

The forces acting on the thrombus surface, possibly

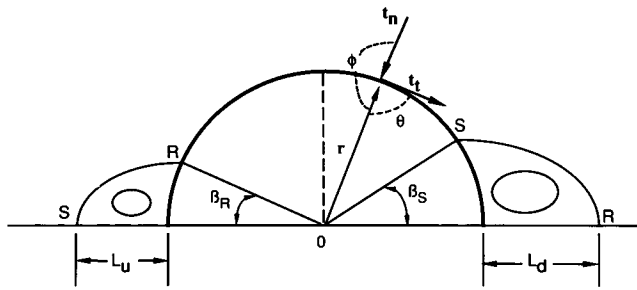


FIGURE 3 Definition sketch of the standing vortices developing around a semicircular model thrombus. *S*, separation point; *R*, reattachment point. The normal and tangential components of the stress vector, t_n and t_t , are also shown.

leading to embolization of the aggregate, were estimated as a function of Reynolds number (*Re*), model thrombus geometry and size. By definition, the total force acting on the object is the surface integral of all normal and shearing stresses acting on it. The component of the resultant force parallel to the undisturbed initial velocity is called the drag *D*, while the component perpendicular to that direction is called the lift *L* (29). The dimensionless coefficients for lift (C_L) and drag (C_D) were calculated according to:

$$C_D = \frac{\int_{\eta} t_x d\eta}{0.5 \rho U^2 h}; \quad C_L = \frac{\int_{\eta} t_y d\eta}{0.5 \rho U^2 h}, \quad (3)$$

where *U* is the velocity of the undisturbed flow at the top of the object; *h* is the object height; t_x and t_y are respectively, the *x* and *y* components of the stress vector;

and η represents the path along the object boundary. The moment coefficient (C_M), defined as the dimensionless torque acting on the object, was also computed according to:

$$C_M = \frac{\int_{\eta} r t_n \sin \phi d\eta + \int_{\eta} r t_t \sin \theta d\eta}{0.5 \rho U^2 h^2}, \quad (4)$$

where *r* is the distance between the origin and the point of action of the force; θ is the angle between t_t and *r*; and ϕ is the angle between t_n and *r* (see Fig. 3). It should be pointed out that, for geometrically similar objects, those dimensionless coefficients are functions of one parameter only, the Reynolds number. In other words, for a given thrombus geometry, the thrombus size is not a variable (29).

The average basal shear stress ($\bar{\tau}_s$) and average basal tensile or normal stress ($\bar{\tau}_n$) were also computed according to:

$$\bar{\tau}_s = C_D 0.5 \rho U^2 h / L \quad \text{and} \quad \bar{\tau}_n = C_L 0.5 \rho U^2 h / L, \quad (5)$$

where *L* represents the object diameter in the case of a semicircular model thrombus, and the object length in the case of a rectangular one.

Estimation of the model parameters

The model parameters for the platelet-activating agents and the chemical reactions, as well as the shear-rate dependent physical parameters are summarized in Tables 1 and 2, respectively. Those parameters were either

TABLE 1 Model parameters for the platelet-activating agents and the chemical reactions

Chemical species	Molecular weight	Brownian diffusion coefficient, D_b^*	Pseudo 1 ^o order reaction rate constant, <i>k</i>	Amount per platelet**	Initial whole blood concentration**
	<i>daltons</i>	<i>cm²/s</i>	<i>s⁻¹</i>		
ADP	424.2	2.57×10^{-6}	—	2.4×10^{-17} mol	0.000
TxA ₂	352.5	2.14×10^{-6}	0.0161^{\ddagger}	0.95×10^{-20} mol/s	0.000
Prothrombin	72000	3.32×10^{-7}	—	—	0.869 μ M
Thrombin	36600	4.16×10^{-7}	—	—	0.000
Antithrombin III	62000	3.49×10^{-7}	0.0201^{\S}	—	2.844 μ M
Heparin	16000	—	$11.850^{\ } 127.0^{\ }$	—	—
vWF	—	1.20×10^{-7}	—	0.2×10^{-9} U	0.608 U/ml

*See references 15, 51.

[†]For the nonenzymatic hydrolysis of TxA₂ to TxB₂ (see reference 15).

[‡]For the inhibition of thrombin by 2.844 μ M AT III alone.

[§]For the inhibition of thrombin by 2.844 μ M AT III accelerated by 2.0833 μ M heparin (300 USP units/mg), the experimentally used concentration.

^{||}For the inhibition of thrombin by 2.844 μ M AT III accelerated by 0.09 μ M heparin, the concentration for maximum rate of inhibition.

**See references 51, 52.

**Assuming an average hematocrit of 39.2%.

TABLE 2 Shear rate dependent parameters

Wall Shear Rate	Apparent Viscosity, μ^*	Enhanced Diffusion Coefficient, D_1^\ddagger	Reynolds number [§] (Re)
s^{-1}	cp	cm^2/s	
100	4.223	1.36×10^{-6}	0.178
800	3.405	1.09×10^{-5}	1.770
1500	3.288	2.04×10^{-5}	3.436

*See reference 55.

‡Calculated from Eq. C3.

§ $Re = \rho V_{max} B/\mu$.

obtained from the literature or estimated as shown in Appendix C.

The experimental data on thrombus growth rates and sizes, as well as the estimated platelet-activating agent wall fluxes are summarized, as a function of wall shear rate and thrombus size, for the semicircular and rectangular model thrombi, in Tables 3 and 4, respectively. The details of those flux calculations are also shown in Appendix C.

RESULTS AND DISCUSSION

The effects of viscous shear flow on the mechanics of thrombus growth and embolization, as well as the concentration profiles of four potential platelet-activating substances generated in the vicinity of various model thrombi, were estimated at various wall shear rates, spanning the physiological range. The reasons for taking the effect of wall shear rate into account and for choosing two particular model thrombus geometries in this study, were obtained from the following experimental observations. A pseudo-color enhanced representation of three-dimensional reconstructions of thrombi formed after 120 s of blood flow at $1,500 s^{-1}$ over a human collagen-coated surface is shown in Fig. 4. As can be observed from that figure, the actual thrombi have steep edges, are irregularly shaped on the top, and are elongated in the flow direction. These thrombi could well be imagined as hav-

ing contours shaped between that of a perfect semicircle and that of a perfect rectangle. Similarly, Fig. 5 shows three-dimensional reconstructions of thrombi formed after 120 s of flow at three different wall shear rates, $1,500 s^{-1}$, $800 s^{-1}$, and $100 s^{-1}$. This figure illustrates, in a qualitative manner, the fact, observed by others (30), that the rate of platelet accumulation on a thrombogenic surface increases with increasing wall shear rate, resulting in thrombi of different sizes. Because the wall fluxes of all platelet-activating agents depend primarily on the rate of thrombus growth or the thrombus size itself, it was therefore necessary to consider the effect of wall shear rate when estimating those fluxes in this study.

Effects of viscous shear flow

Although the problems of a circular cylinder and a sphere exposed to a uniform shear flow are well-known ones in fluid mechanics (29, 31), the situation of a small object attached to a plane wall in a uniform viscous shear flow has been considered by relatively few investigators. (32–34). Therefore, our objective was to study quantitatively the effects of viscous shear flow on a growing thrombus as a function of wall shear rate and model thrombus size and geometry, and to discuss the implications of those effects with respect to the thrombogenesis mechanism.

The schematic definition of the standing vortices developing upstream and downstream of a growing thrombus as a result of viscous shear flow is given in Fig. 3. The lengths L_u and L_d of the upstream and downstream vortices, respectively, as well as the reattachment angle β_R and the separation angle β_S , are shown in Table 5 as a function of the particle Reynolds number R_h and model thrombus. In general, our results confirm the predictions made by Kiya and Arie (32) and, also shown by Mills (34) for creeping flow ($R_h \leq 0.1$) over a square-edged orifice plate in a circular pipe, that standing vortices do develop upstream and downstream of the obstacle even in the limit $R_h \rightarrow 0$. This is in contrast to the case of a circular cylinder or a sphere in a uniform shear flow, for which a separated region with back-flow appears behind the object when the Reynolds number approaches 3.5 for

TABLE 3 Model parameters for the circular model thrombi

Diameter	Wall shear rate	Time	Thrombus growth rate	Thrombus size	ADP flux	TxA ₂ flux	Thrombin flux	vWF flux
μm	s^{-1}	s	$platelet/s$	$platelets$	$mol/\mu m^2 s \times 10^{20}$	$mol/\mu m^2 s \times 10^{21}$	$U/\mu m^2 s \times 10^9$	$U/\mu m^2 s \times 10^{12}$
10	100	83.68	2.27	44.9	34.7	2.71	0.90	2.9
	800	12.17	3.55	28.2	54.3	1.71	6.80	4.5
	1500	19.16	3.04	26.1	46.5	1.58	12.6	3.9
20	100	130.32	2.87	170.4	11.0	2.57	1.30	0.9
	800	109.95	2.63	209.3	10.1	3.16	10.1	0.8
	1500	55.500	6.76	209.4	25.8	3.17	18.8	2.2

TABLE 4 Model parameters for the rectangular model thrombi

Length	Height	Width	Wall shear rate	Time	Thrombus growth rate	Thrombus size	ADP flux	TxA ₂ flux	Thrombin flux	vWF flux
μm	μm	μm	s^{-1}	s	platelet/s	platelets	$\text{mol}/\mu\text{m}^2\text{s} \times 10^{20}$	$\text{mol}/\mu\text{m}^2\text{s} \times 10^{21}$	$\text{U}/\mu\text{m}^2\text{s} \times 10^9$	$\text{U}/\mu\text{m}^2\text{s} \times 10^{12}$
10	5	7.5	100	89.07	2.41	57.5	23.2	2.18	0.90	1.9
			800	15.48	3.28	39.5	31.5	1.50	7.10	2.6
			1500	22.63	3.47	37.5	33.2	1.42	13.2	2.8
20	10	15	100	143.00	2.79	206.3	6.70	1.96	1.40	0.6
			800	135.56	4.84	302.7	11.6	2.87	10.8	1.0
			1500	68.030	7.66	300.0	18.4	2.85	20.0	1.5

the former (32) and 20 for the latter (29). The data presented in Table 5 indicate that L_u and β_R decrease slightly with increasing R_h , while L_d and β_S increase slightly with increasing R_h , which is consistent with the data presented in Figs. 7 and 8 by Kiya and Arie (32). Whereas their data show that for large R_h the downstream vortex is always much larger than the upstream one, our data reveal that both standing vortices become geometrically similar as $R_h \rightarrow 0$. The size of both recirculation regions is strongly dependent upon the model thrombus geometry, as indicated by the relatively large standing vortices formed with rectangular model thrombi compared to those formed with semicircular ones. The most interesting result, however, appears in the

case of two rectangular thrombi growing near each other and separated by a distance equal to one thrombus length or 20 μm . Indeed, as shown by the streamlines in Fig. 6 *b* and the data in Table 5, a large standing vortex, 20 μm long and 8–9 μm high, develops between the two thrombi at all wall shear rates investigated. On the other hand, this large vortex is not present when the thrombi are separated by 10 times a thrombus length or 200 μm (see Table 5).

Another effect of viscous shear flow is the nonuniform fluid velocity distribution across the channel, and in particular, the considerably reduced velocities in and near the recirculating regions. This effect is shown graphically by the velocity vector plot of Fig. 6 *a*, where the direction

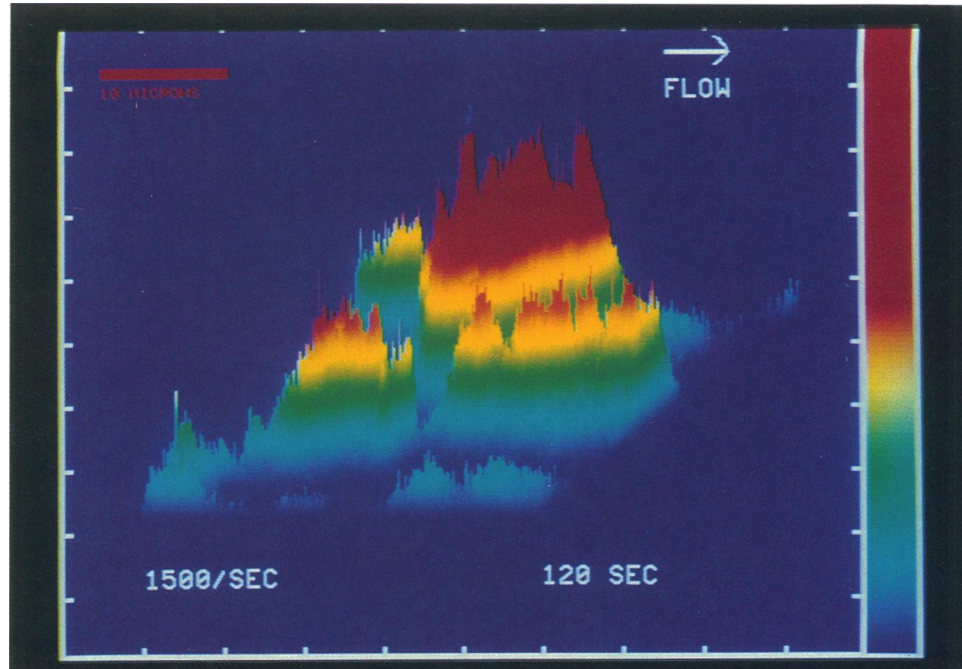


FIGURE 4 Estimation of the three-dimensional structures of thrombi formed after 120 s of blood flow at 1,500 s^{-1} over a type I human collagen-coated glass cover slip in a parallel plate flow chamber. Flow is from left to right. The length bar applies to both the length and the height of the thrombi. Light blue represents the bottom of the thrombi, whereas red represents the top.

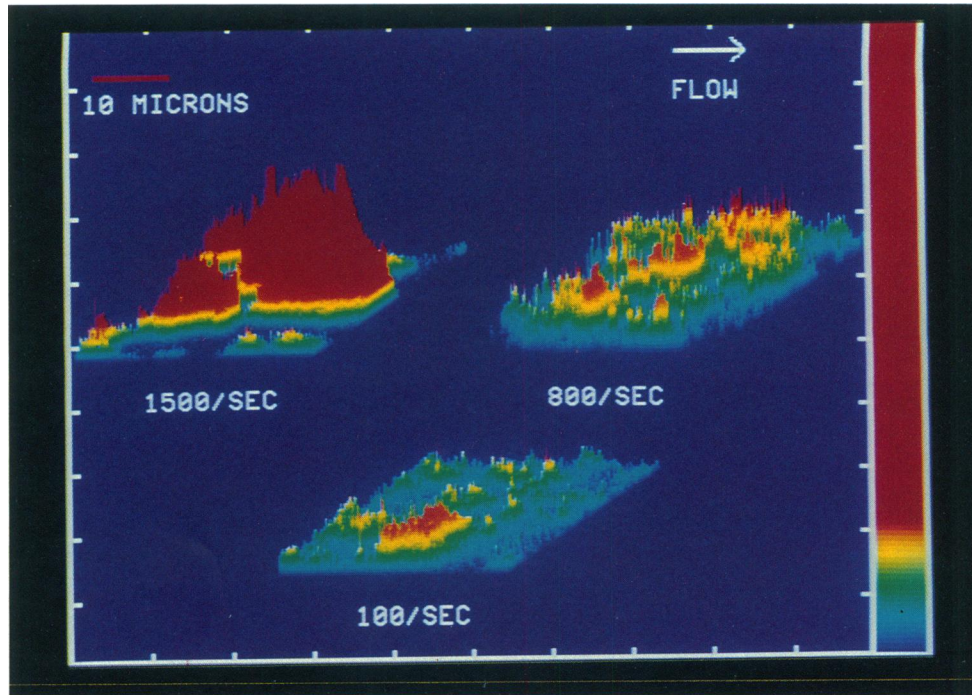


FIGURE 5 Effect of wall shear rate on the kinetics of thrombus growth. The same comments as those in Fig. 4 apply.

and the length of the arrow represent, respectively, the direction and magnitude of the velocity vectors, plotted at each nodal point. From that figure, one can see that the velocity components in the recirculating wake regions and their surroundings, as well as in the fluid layer directly

above the thrombi, are very small when compared to those in the bulk. In fact, at $1,500 \text{ s}^{-1}$, the smallest velocity vector estimated has a magnitude of 0.0375 cm/s , while the speed of the entering fluid at the top of the objects, U , is 1.425 cm/s . Similarly, at 100 s^{-1} , the smallest calcu-

TABLE 5 Sizes of the standing vortices as a function of Reynolds number and model thrombus

	R_h	Semicircle $L = 10 \mu\text{m}$	Rectangle $L = 10 \mu\text{m}$	R_h	Semicircle $L = 20 \mu\text{m}$	Rectangle $L = 20 \mu\text{m}$	$D = 20 \mu\text{m}$		$D = 200 \mu\text{m}$	
							A	B	A	B
L_u	0.016	0.980	3.640	0.064	1.780	3.470	4.860	20.000	4.880	2.830
	0.008	0.990	3.670	0.033	1.820	3.500	4.870	20.000	4.890	2.940
	0.001	1.060	3.760	0.003	1.920	3.600	4.880	20.000	4.900	3.260
L_d	0.016	1.020	4.470	0.064	1.950	3.630	20.000	7.830	3.200	7.900
	0.008	1.010	4.450	0.033	1.910	3.570	20.000	7.750	3.120	7.720
	0.001	0.990	4.410	0.003	1.850	3.490	20.000	7.610	3.060	5.960
β_R	0.016	4.900	35.700	0.064	4.120	34.900	28.410	41.700	28.620	36.500
	0.008	5.000	35.800	0.033	4.260	35.070	28.530	41.740	28.990	36.750
	0.001	5.660	36.100	0.003	4.740	35.460	28.670	41.800	29.280	38.050
β_S	0.016	5.350	29.700	0.064	4.900	30.850	38.800	30.000	32.200	29.820
	0.008	5.210	29.670	0.033	4.630	30.720	38.760	29.890	32.640	29.670
	0.001	4.900	29.600	0.003	4.320	30.470	38.800	29.760	32.420	29.720

L_u and L_d are given in μm , whereas β_R and β_S are given in degrees. For comparison, the Reynolds number is defined as in reference 32, namely, $R_h = Uh\rho/\mu$, where U is the undisturbed velocity at the top of the object, and h is the height of the object.

*Two $20\text{-}\mu\text{m}$ -long rectangular model thrombi separated by a distance of $20 \mu\text{m}$.

†Two $20\text{-}\mu\text{m}$ -long rectangular model thrombi separated by a distance of $200 \mu\text{m}$.

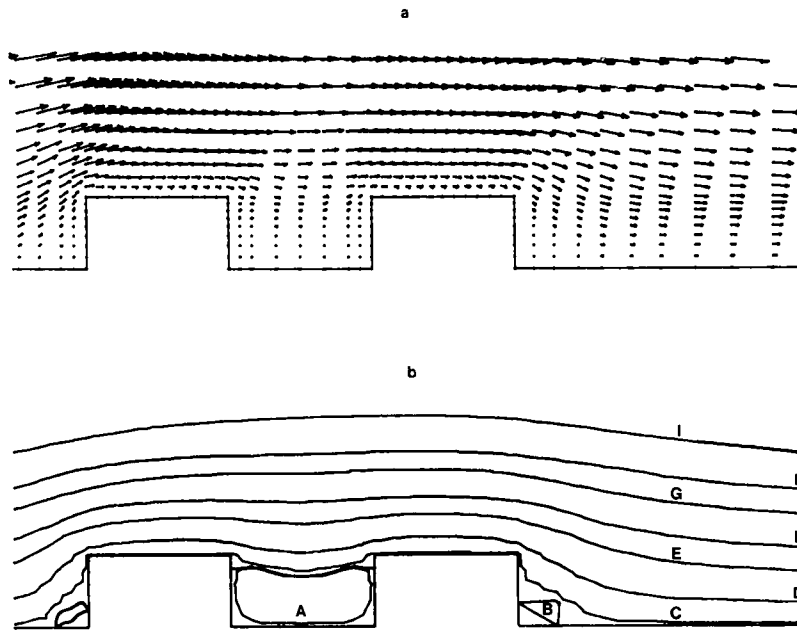


FIGURE 6. Velocity vector plot (a) and streamlines (b) in the case of two nearby-growing rectangular model thrombi $20\ \mu\text{m}$ long at $Re = 0.178$. In a, the direction and length of the arrows represent, respectively, the direction and magnitude of the velocity vectors, plotted at each nodal point. In b, the values for the dimensionless stream function Ψ^* (where $\Psi^* = \Psi/V_{\max}B$) are: $A = 0.16 \times 10^{-4}$, $B = 0.0$, $C = 0.10 \times 10^{-3}$, $D = 0.10 \times 10^{-2}$, $E = 0.50 \times 10^{-2}$, $F = 0.10 \times 10^{-1}$, $G = 0.20 \times 10^{-1}$, $H = 0.30 \times 10^{-1}$, $I = 0.50 \times 10^{-1}$.

lated speed in the vortex region is $\sim 2.5 \times 10^{-3}$ cm/s, while U is 95×10^{-3} cm/s.

The drag coefficient C_D , the lift coefficient C_L , and the moment coefficient C_M , decrease more or less linearly with the Reynolds number R_h , when plotted on a logarithmic scale, as shown in Fig. 7. Most noteworthy is that C_D and C_M are always larger for the rectangular model thrombus than for the semicircular one, whereas C_L is independent of thrombus geometry for $R_h > 0.003$. The differences in C_D values between the semicircular and the rectangular protrusions are relatively small, however. This was also reported by Basmadjian (35), who noticed that C_D values for small protrusions of different shapes differed little over the full range of viscous flow. When extrapolating the values of C_D and C_M obtained for the semicircular projection to $R_h = 0.1$, our results agree reasonably well with those obtained by Kiya and Arie (32). Indeed, from the data of Fig. 7, C_D and C_M are 160 and 80, respectively, at $R_h = 0.1$, compared to 170 and 100 from Figs. 12 and 13 of Kiya and Arie (32). Also shown in Fig. 7 is the case of two nearby-growing thrombi. For that particular situation, C_D and C_M are always larger for the upstream thrombus (A) than for the downstream one (B), while the same values are found for C_L .

The average stresses and the torque acting on the

aggregate as it grows under the effects of viscous shear flow, eventually leading to its embolization from the wall surface, are summarized in Table 6, as a function of wall shear rate and model thrombus. Both shear stress and normal stress, as well as the torque, increase with increasing wall shear rate, as normally expected. On the other hand, the embolizing stresses are insensitive to thrombus dimension. This was also shown empirically by Basmadjian (35), who found that in both creeping flow regime ($R_h \leq 0.1$) and for sufficiently small protrusions ($h/2B \leq 0.05$), shear stress and tensile stress are independent of object height. Our numerical results for the average shear stress $\bar{\tau}_s$ agree within 25–30% with the values predicted by a semi-empirical equation derived by Basmadjian (35) ($\bar{\tau}_s = 30\mu \langle V \rangle^2/2B$, where $\langle V \rangle$ equals $\frac{2}{3}V_{\max}$ and represents the average fluid velocity across the channel). Also shown in Table 6 is the slightly larger average shear stress acting on the rectangular object compared to the one acting on the semicircular object, whereas the average normal stresses are similar for both geometries. In the case of two nearby-growing thrombi, the average shear stress and the torque acting on the downstream thrombus (B) are reduced by $\sim 25\%$ when compared with those acting on the upstream one (A), which could favor the growth of the former aggregate. Again, the average normal stresses are similar for both

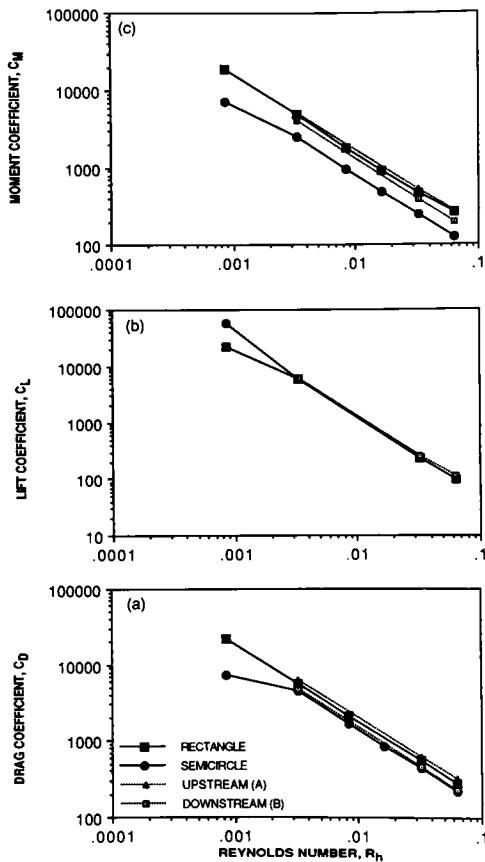


FIGURE 7 Drag coefficient C_D , lift coefficient C_L , and moment coefficient C_M as a function of the Reynolds number R_h , defined in terms of the undisturbed velocity at the top of the object U and the height of the object h as $R_h = Uh\rho/\mu$. Solid lines are used for single rectangular or semicircular model thrombi, whereas dashed lines are used for two nearby-growing rectangular model thrombi.

thrombi. It is interesting to notice that at the low wall shear rate of 100 s^{-1} both shear stress and normal stress have relatively similar values, while, as the wall shear rate increases, the shear stress becomes the predominant embolizing stress. As distinct from the stresses, the torque is not only a function of thrombus geometry but also a function of thrombus size.

Fig. 8 shows four pseudo-color enhanced images of growing thrombi, digitized after, respectively, 30, 75, 105, and 120 s of blood flow over a collagen-coated surface. This photograph explicitly shows that the large zones of recirculation and back-flow (indicated by blue crosses) developing between nearby-growing thrombi at particular stages in the thrombosis process are also the sites of massive platelet aggregation at later stages. The region of recirculation present near the center of Fig. 8 A, for instance, is completely covered with platelets 45 s later, as indicated at the same location in Fig. 8 B.

Concentration profiles of platelet-activating agents

The concentration profiles of released platelet-activating agents are presented as three-dimensional plots in this paper (see Fig. 10 for example), and those require a few comments. The x - y plane in those figures represent the actual channel geometry as drawn in Fig. 1, while the concentration variation of the substance of interest over that two-dimensional space is represented by the third dimension (c axis). Blood is flowing in the positive x -direction, that is, from right to left. All those figures also exhibit two local maxima (labeled 1 and 2), and one local minimum, upstream and downstream from the thrombus and near the top of the thrombus, respectively. The presence of local maxima is related to the standing vortices which develop on both sides of the aggregate, as mentioned earlier. Indeed, because those recirculating regions are areas of low fluid velocities, the retention time of any released material, and thereby its concentration, is correspondingly larger in those regions. Although the fluid velocities near the top of the aggregate are considerably smaller than those in the bulk, as shown previously, they are, however, larger than those within the vortices, which explains the presence of a local minimum in that region. In fact, as one moves away from the wall or the aggregate surface into the bulk, the convective dispersion rapidly becomes important, resulting in steep decreasing concentration gradients. Therefore, only platelets that flow in close proximity to the thrombus surface or the wall surface have a chance to become activated, and subsequently to aggregate, either by being trapped in the vortex regions or by flowing directly within the zone of high concentration of platelet-activating agents present near the top of the thrombus. It should be pointed out that the downstream maximum is always larger than the upstream one, which can be explained as follows: some of the molecules released from the upstream part or the top of the thrombus are carried along by convection in the direction of the downstream vortex, increasing the local concentration there. This theoretical result correlates well with previous experimental observations made in our laboratory (19, 24, 36). Indeed, it was postulated that "fresh" platelets arriving at the site of aggregation become activated as they pass through a "cloud" of platelet-activating agents surrounding the thrombus, and therefore adhere preferentially at the downstream edge of the aggregate. In addition, as will be shown below, the concentrations of platelet-activating agents accumulating in the vortices present between nearby growing thrombi, are significantly larger than those found in the vicinity of isolated thrombi. This result may also explain the experimental observation mentioned earlier in this report, that platelets aggregate massively in the spaces between adjacent thrombi.

TABLE 6 Average shear and normal stresses, and the torque, as a function of wall shear rate and model thrombus

Stress*	Wall shear rate	Semicircle $L = 10 \mu\text{m}$	Semicircle $L = 20 \mu\text{m}$	Rectangle $L = 10 \mu\text{m}$	Rectangle $L = 20 \mu\text{m}$	$D = 20 \mu\text{m}$	
						A	B
	s^{-1}						
Shear stress $\bar{\tau}_s$	100	15.0	15.5	20.0	19.5	21.0	16.5
	800	95.0	94.5	117.0	118.5	137.0	99.0
	1500	171.0	170.5	213.0	214.5	250.5	177.5
Normal stress $\bar{\tau}_n$	100	25.5	20.0	20.0	20.0	20.5	21.0
	800	43.0	49.5	43.0	49.0	55.0	56.0
	1500	65.0	74.5	71.0	73.0	86.5	86.0
Torque $\times 10^3$	100	0.003	0.017	0.009	0.033	0.035	0.028
	800	0.027	0.106	0.051	0.204	0.228	0.168
	1500	0.049	0.192	0.092	0.412	0.417	0.302

*All stresses are given in dynes per square centimeter and the torque in dynes-centimeter.

ADP

Shown in Fig. 9 is the maximum ADP concentration (in micromolar) as a function of wall shear rate and model thrombus. As can be seen from that figure, the maximum ADP concentration increases with decreasing wall shear rate. This can also be visualized by comparing the three-dimensional plots of Figs. 10 and 11 for the $10 \mu\text{m}$ -long semicircular model thrombus at $100 s^{-1}$ and $1,500 s^{-1}$,

respectively. The curves in the upper left-hand corners of those figures represent the variation of the ADP concentration at the wall as a function of axial position in the channel. The points labelled 1 and 2 correspond to the two maxima on the 3-D plots, and are located, respectively, at the upstream and downstream intersections between the bottom plate of the channel and the model thrombus. At $100 s^{-1}$ the larger maximum has a value slightly above $4.5 \mu\text{M}$, while at $1,500 s^{-1}$ it is only $\sim 0.75 \mu\text{M}$, which

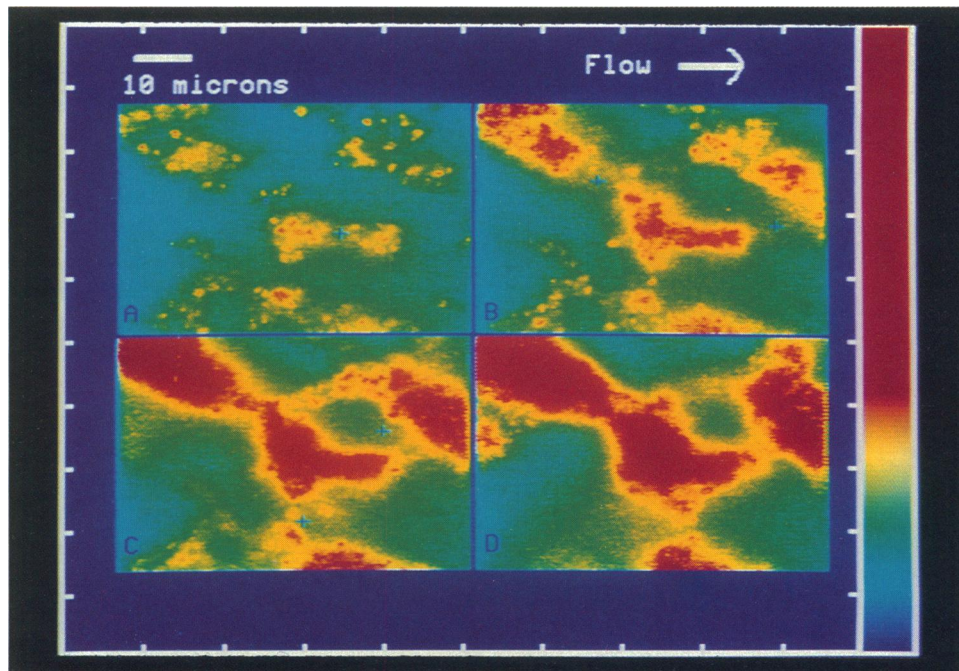


FIGURE 8 Pseudocolor enhanced images of mural thrombi digitized after 30 s (A), 75 s (B), 105 s (C), and 120 s (D) of blood flow over a collagen-coated surface at $1,000 s^{-1}$. The fluorescence intensity ranging from black to white in the original monochrome video image is mapped into a transition from blue to red, where blue represents the surface background and red the regions of intense platelet accumulation. The blue crosses, in that figure, indicate the location of possible standing vortices developing between growing thrombi.

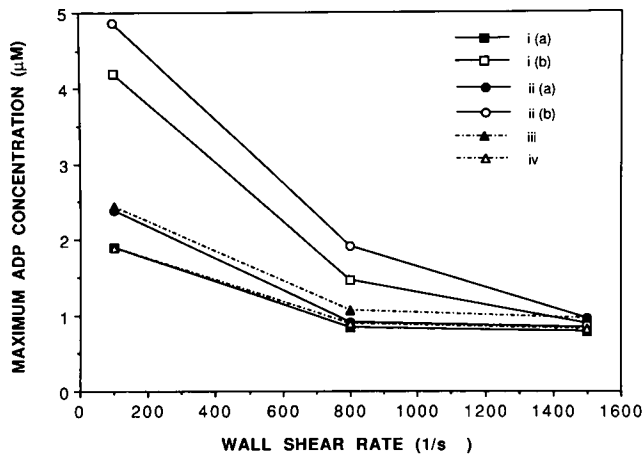


FIGURE 9 Maximum ADP concentration as a function of wall shear rate and model thrombus. Solid lines are used for single thrombi, whereas dashed lines for two thrombi. A similar notation to the one of Fig. 2 is used for designating the different model thrombi: (i) rectangular model thrombus, (a) $L = 20 \mu\text{m}$, (b) $L = 10 \mu\text{m}$; (ii) semicircular model thrombus, (a) $L = 20 \mu\text{m}$, (b) $L = 10 \mu\text{m}$; (iii) two rectangular model thrombi, $L = 20 \mu\text{m}$, $D = 20 \mu\text{m}$; (iv) two rectangular model thrombi, $L = 20 \mu\text{m}$, $D = 200 \mu\text{m}$. L represents the thrombus length or diameter, and D the distance separating the thrombi.

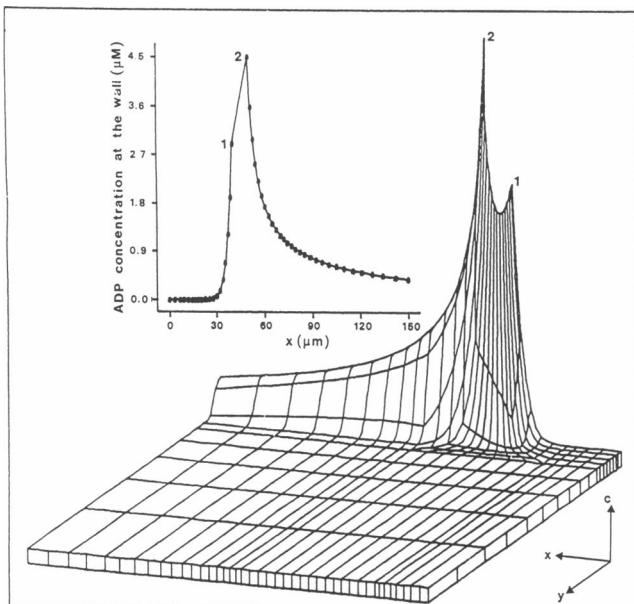


FIGURE 10 ADP concentration profile over a semicircular model thrombus $10 \mu\text{m}$ in diameter. Whole blood flows from right to left at a wall shear rate of 100 s^{-1} . The x - y plane represents the actual channel geometry with the wall at $y = 0$, whereas the height at any nodal point in the x - y plane corresponds to the magnitude of the ADP concentration at that point.

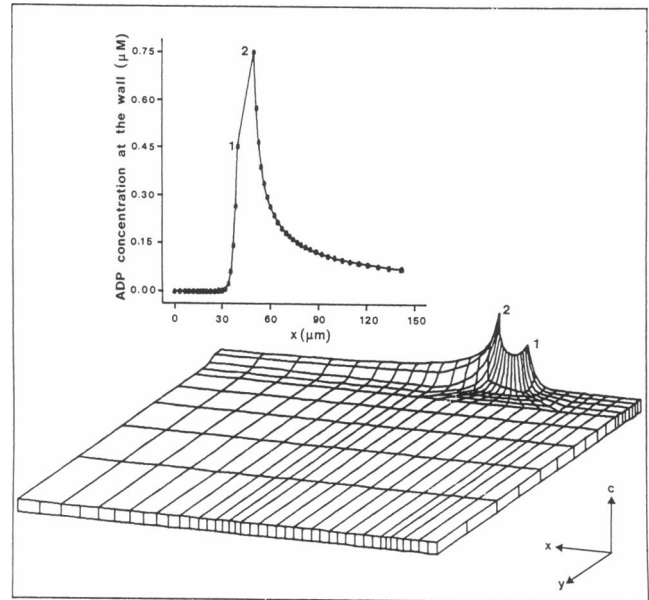


FIGURE 11 ADP concentration profile over a semicircular model thrombus $10 \mu\text{m}$ in diameter. Whole blood flows from right to left at a wall shear rate of $1,500 \text{ s}^{-1}$. The same comments as those of Fig. 10 apply.

corresponds approximately to a decrease of 83% due to the increase in wall shear rate. This decrease in ADP concentration with increasing shear rate is due to both larger convective and diffusive forces at the high shear rate, which tend to reduce the residence time of ADP molecules around the aggregate despite the increase in flux (see Tables 3 and 4). Our results are considerably larger than those found in the case of a flat model thrombus (15). Indeed, values of $0.7 \mu\text{M}$ and $0.32 \mu\text{M}$ were reported for flow over a flat $10\text{-}\mu\text{m}$ -long thrombus at 100 s^{-1} and $1,500 \text{ s}^{-1}$, respectively. These differences are due first to the presence of large vortices in our simulation and second, to the fact that ADP fluxes were underestimated in the previous analysis.

Whereas thrombus size or geometry does not seem to affect, to any significant extent, the maximum ADP concentration at high wall shear rates, it certainly does at low wall shear rates, as shown in Fig. 9. In general, the maximum ADP concentration is larger for a semicircular model thrombus than for a rectangular one, and it decreases with increasing size. At 100 s^{-1} , for instance, the maximum ADP concentration for the $10 \mu\text{m}$ -long semicircular model thrombus is slightly above $4.5 \mu\text{M}$, as mentioned earlier, while it is only around $2.5 \mu\text{M}$ for the $20\text{-}\mu\text{m}$ -long one. It should be stressed, however, that this value is still somewhat larger than the $0.90 \mu\text{M}$ reported for a $20\text{-}\mu\text{m}$ -long flat thrombus (15). The reason for that decrease is that the ADP flux from the aggregate surface

depends upon the rate of platelet arrival to that surface. Although the rate of platelet arrival, as determined experimentally, is greater for rectangular model thrombi than for semicircular ones, and increases slightly with increasing thrombus size, the rate of arrival per unit area is smaller for large thrombi and/or rectangular ones because of their larger surface area, especially at low shear rates (see Tables 3 and 4).

As shown in Fig. 12 B, the region of recirculation and back-flow developing between two nearby-growing 20- μm -long rectangular thrombi is also a zone of local high ADP concentration. This is not present, however, in the case of two similar thrombi separated by ten times the same distance, as shown in Fig. 12 A. In fact, at 100 s^{-1} , the maximum ADP concentration increases by 22%, when compared to the case of a single growing thrombus or of two distant thrombi of the same size. As shown quantitatively in Fig. 9, this effect increases with decreasing wall shear rate.

As reported by others (37), the level of ADP required to cause platelet shape change and irreversible aggregation in platelet-rich-plasma (PRP) is 0.2 μM and 1.0 μM , respectively. Our results lie in the region of the minimum threshold for irreversible platelet aggregation. It is likely, however, that as the wall shear rate and thrombus size increase, the maximum ADP concentration could decrease below that minimum. In other words, ADP is likely to play its most important role in the thrombogene-

sis process at low shear rates, typical of the venous system, and during the early stages of the process, when aggregate sizes are relatively small.

TxA₂

The variation of the maximum TxA₂ concentration (in nmolar) with wall shear rate is shown in Fig. 13 for different model thrombi. As for ADP, the maximum TxA₂ concentration increases with decreasing wall shear rate. This is also shown qualitatively in Fig. 14 for the 20- μm -long rectangular model thrombus, for which the maximum TxA₂ concentration passes from 12.9 nM at 1,500 s^{-1} , to 20.9 nM at 800 s^{-1} , and to 61.2 nM at 100 s^{-1} , corresponding to a total increase of 79%. The maximum TxA₂ concentration increases with increasing thrombus size, and does not vary much with thrombus geometry (see Fig. 13). The former observation is basically due to the fact that the TxA₂ flux from the thrombus surface depends on the total number of platelets constituting that thrombus, and not on the rate of platelet arrival to the thrombus, as is the case for ADP. The latter observation is a result of the relatively similar fluxes estimated for the rectangular and semicircular model thrombi, as shown in Tables 3 and 4. Also shown in Fig. 13 is the significant increase in maximum TxA₂ concentration in the case of two nearby-growing thrombi when compared to a single thrombus or of two distant thrombi of the same size, especially at low shear rate. At 100 s^{-1} , for instance, that increase is ~21.2%.

In general, our values for the maximum TxA₂ concentrations are smaller than those reported earlier for the flow over a flat thrombus (15). For example, the maxi-

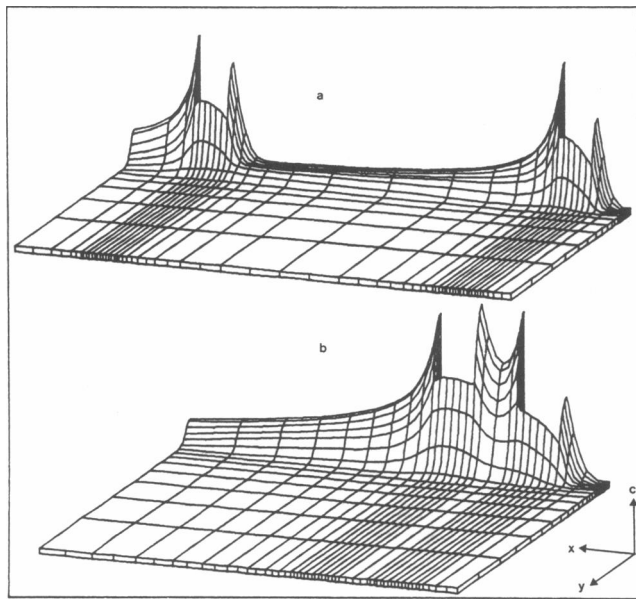


FIGURE 12 ADP concentration profile over (a) two 20- μm -long rectangular model thrombi 200 μm apart, (b) two 20- μm -long rectangular model thrombi 20 μm apart. Whole blood flows from right to left at a wall shear rate of 100 s^{-1} .

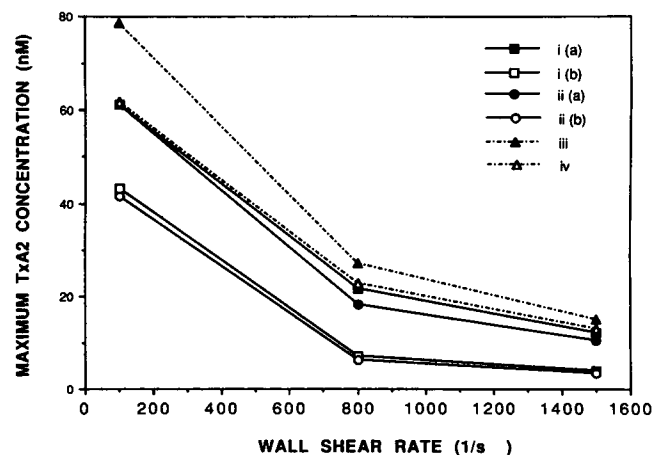


FIGURE 13 Maximum TxA₂ concentration as a function of wall shear rate and model thrombus. The notation is similar to the one used in Fig. 9.

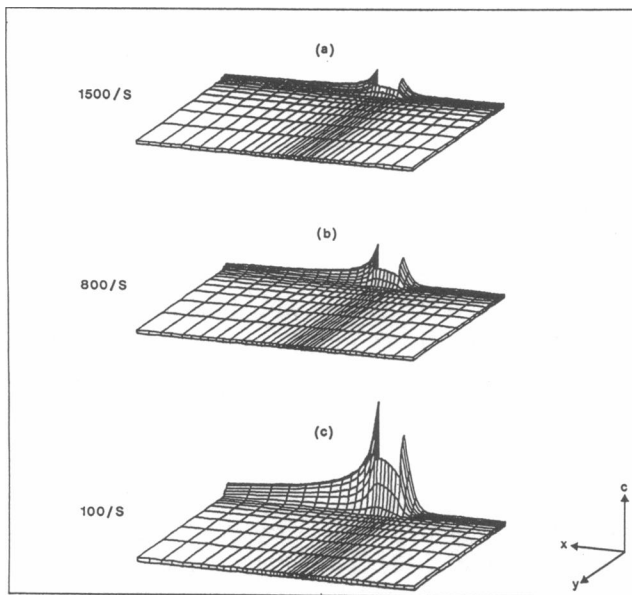


FIGURE 14 Effect of wall shear rate on TxA_2 concentration profile over a $20\text{-}\mu\text{m}$ -long rectangular model thrombus: (a) $1,500\text{ s}^{-1}$; (b) 800 s^{-1} ; (c) 100 s^{-1} .

imum value found in the case of a $20\text{-}\mu\text{m}$ -long semicircular model thrombus at 100 s^{-1} is slightly above 60 nM , whereas the same value was reported to be $\sim 200\text{ }\mu\text{M}$ in the case of a flat thrombus. This apparent discrepancy is mostly due to overestimation of the TxA_2 fluxes, especially for the large aggregates, reported in the case of a flat thrombus.

Because TxA_2 has a short half-life in aqueous solution, it is difficult to determine what TxA_2 concentrations are needed to stimulate platelet activity in vitro. Therefore, it

is assumed, as mentioned by others (15), that the biological behavior of TxA_2 is similar to the one of its close analogue, U-46619 (11,9-epoxy-methano analogue of PGH_2 , Upjohn Company), which causes shape change at concentrations of $6\text{--}60\text{ nM}$, reversible aggregation at $110\text{--}300\text{ nM}$, and irreversible aggregation at concentrations $>600\text{ nM}$ (38). According to those numbers, the concentrations calculated for TxA_2 are only sufficient to cause platelet shape change. It is possible that, as the thrombus grows larger, enough TxA_2 will be released to cause reversible platelet aggregation. On the other hand, it is very unlikely that TxA_2 alone could induce irreversible platelet aggregation. Those results confirm the experimental data reported by Baumgartner (39) who showed that preventing TxA_2 generation by blocking cyclooxygenase activity with aspirin caused little change in thrombus formation in heparin anticoagulated or native rabbit blood on subendothelium.

Thrombin

The maximum thrombin concentration is presented in Table 7 as a function of wall shear rate, heparin concentration, and model thrombus geometry. Thrombin is known to cause irreversible platelet aggregation at levels of $0.1\text{--}0.3\text{ units/ml}$ in PRP (37). All the values shown in Table 7 are significantly larger than the minimum threshold required for irreversible platelet aggregation. Indeed, the calculated maximum thrombin concentration values range from 279.2 to 21.8 U/ml , both found in the case of two nearby-growing thrombi, respectively, at $1,500\text{ s}^{-1}$ with no heparin and at 100 s^{-1} with $0.09\text{ }\mu\text{M}$ heparin (see Table 7).

The maximum thrombin concentration drops very drastically when thrombin is inhibited by AT III in

TABLE 7 Maximum thrombin concentration[†] as a function of wall shear rate, heparin concentration, and model thrombus

Wall shear rate	Heparin concentration	Semicircle $L = 10\text{ }\mu\text{m}$	Semicircle $L = 20\text{ }\mu\text{m}$	Rectangle $L = 10\text{ }\mu\text{m}$	Rectangle $L = 20\text{ }\mu\text{m}$	$\frac{A}{D}$		$\frac{B}{D}$	
						$D = 20\text{ }\mu\text{m}$	$D = 200\text{ }\mu\text{m}$	$D = 20\text{ }\mu\text{m}$	$D = 200\text{ }\mu\text{m}$
s^{-1}	μM								
1500	0.0000	178.0	210.3	192.7	230.3	279.2	252.6		
	2.0833*	170.7	194.3	181.6	201.9	225.6	222.0		
	0.0900 [‡]	124.1	115.5	119.7	87.8	155.4	144.5		
800	0.0000	176.4	208.0	190.9	227.3	276.5	249.5		
	2.0833	163.5	180.6	171.6	181.1	194.3	199.4		
	0.0900	95.3	102.6	114.1	86.1	72.0	81.4		
100	0.0000	144.8	140.1	156.3	184.1	224.9	202.3		
	2.0833	96.5	92.6	92.3	70.0	72.8	83.3		
	0.0900	30.0	26.8	57.4	22.7	21.8	49.2		

*The experimentally used heparin concentration.

[†]The heparin concentration for maximum rate of inhibition (see reference 25).

[‡]All thrombin concentrations are given in units per milliliter.

presence of heparin. This is shown both quantitatively in Table 7 and qualitatively in Fig. 15 for the 20- μm -long rectangular model thrombus at 800 s^{-1} . In that figure, the maximum thrombin concentration drops from 227.3 U/ml in absence of heparin, as would be found in an unaltered physiological environment (Fig. 15 C), to 86.1 units/ml in presence of $0.09\ \mu\text{M}$ heparin, the concentration at which the enzymatic inactivation of the released thrombin by AT III is maximum (Fig. 15 A) (25). An intermediate value of 181.1 U/ml is found in presence of $2.0833\ \mu\text{M}$ heparin, the experimentally used concentration (Fig. 15 B) (19). Most noteworthy in Fig. 15 A is the lack of a concentration tail downstream of the aggregate, as well as the small peaks on both sides of the thrombus, when compared to Fig. 15 C. Those results are a consequence of the rapid inactivation of thrombin molecules, as they are released from the aggregate, by the circulating AT III molecules when heparin is present. In fact, the AT III molecules present in the standing vortices keep large quantities of thrombin molecules from accumulating in those regions, thereby reducing considerably the size of the two concentration maxima. Furthermore, because of this rapid inactivation reaction, thrombin molecules have no chance to diffuse away from the wall or to be carried by convection downstream from the aggregate. At $3\ \mu\text{m}$ from the wall, for instance, the maximum thrombin

concentration drops to 0.051 and 0.018 U/ml in Figs. 15, C and A, respectively, which correspond to a 4,457- and 4,783-fold decrease when compared to the maximum values at the wall.

The effect of wall shear rate on the maximum thrombin concentration is also shown in Table 7. In general, that value decreases with decreasing shear rate, and this effect is particularly noticeable when the rate of thrombin inhibition is accelerated by heparin. For instance, in the case of a 20- μm -long rectangular model thrombus, the maximum thrombin concentration decreases by 20.1% when the wall shear rate decreases from $1,500\text{ s}^{-1}$ to 100 s^{-1} with no heparin present, while that decrease is 74.1% with $0.09\ \mu\text{M}$ heparin. This result can be explained by the fact that the rate of thrombin production increases while its rate of inhibition decreases, with increasing wall shear rate. Indeed, at low wall shear rates, the convective forces near the thrombus surface are relatively small, and the potential residence time of the released thrombin molecules comparatively long. In those conditions, AT III molecules become more effective in inhibiting a large number of thrombin molecules, particularly when the rate of reaction is enhanced by heparin. In addition, the rate of thrombin production increases with increasing wall shear rate because of the increasing diffusive and convective forces carrying prothrombin, the precursor of thrombin, from the bulk to the aggregate surface. This is also shown in Tables 3 and 4 as an increase in thrombin flux with wall shear rate.

Our calculated thrombin concentration values are considerably larger than the values reported for planar thrombi, mainly because the estimated thrombin fluxes were underestimated in the previous analysis (15). In addition, contrary to those previously reported data, our results predict a decrease in thrombin concentration with increasing thrombus size and decreasing wall shear rate, in presence of heparin.

It is clear from our results that thrombin is likely to be the most potent platelet-activating substance, and therefore, should play a profound role in the mechanism of mural thrombogenesis on collagen, even in the presence of heparin. These findings agree well with the very recent data reported by other groups (40–42), which indicate that thrombus formation *in vivo* on damaged blood vessels is a thrombin-mediated, but heparin-resistant, process.

Platelet-released vWF

The maximum vWF multimer concentrations developing in the vicinity of various model thrombi are shown in Fig. 16 at two extreme wall shear rates, 100 s^{-1} and $1,500\text{ s}^{-1}$. For the same reasons as mentioned earlier for ADP, the maximum vWF concentration values increase with decreasing shear rate and thrombus size, are larger for

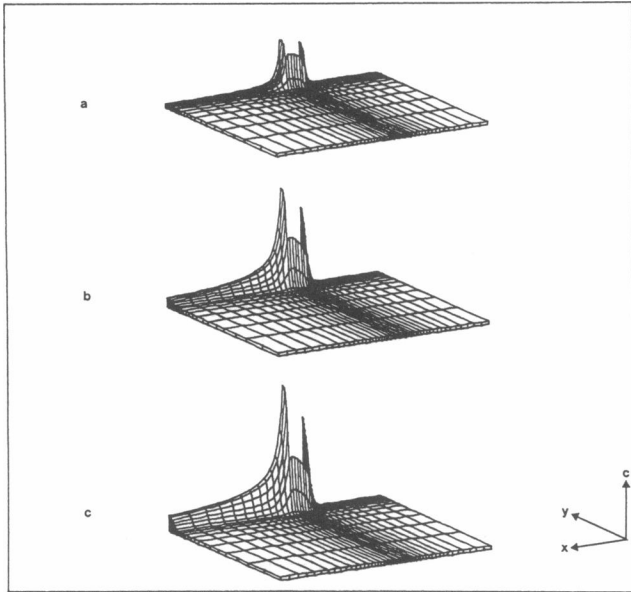


FIGURE 15 Effect of heparin on thrombin inhibition by circulating AT III. The thrombin concentration profiles are shown over a 20- μm -long rectangular model thrombus at 800 s^{-1} . The heparin concentrations in whole blood are as following: (a) $0.09\ \mu\text{M}$ heparin, the concentration for maximum rate of inhibition, (b) $2.0833\ \mu\text{M}$ heparin, the experimentally-used concentration, and (c) no heparin.

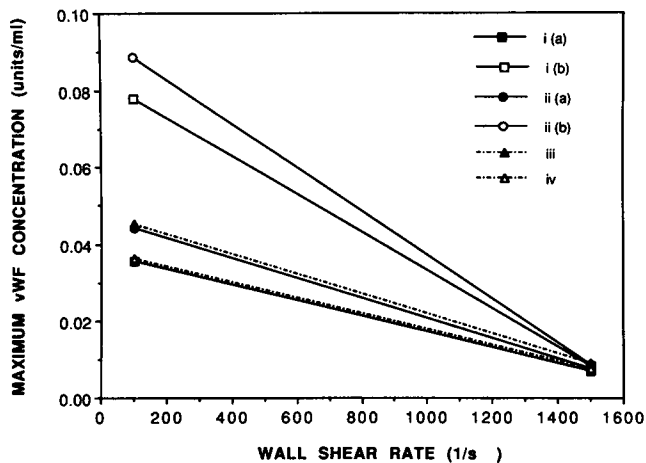


FIGURE 16 Maximum platelet-released vWF multimer concentration as a function of wall shear rate and model thrombus. The notation is similar to the one used in Fig. 9.

semicircular model thrombi than for rectangular ones, and increase in the case of two nearby-growing thrombi, when compared to the case of a single thrombus or of two distant thrombi of the same size. At 100 s^{-1} , for instance, that increase is $\sim 25.0\%$.

The endogenous human platelet vWF multimers include unusually large vWF multimeric forms similar to those released by endothelial cells (ECs) and larger than the largest multimeric forms found in normal human plasma (43). Moake et al. showed that both vWF multimers secreted by ECs and those released by platelets are more effective in inducing shear-induced platelet aggregation than the largest plasma forms (43, 44). Also, the antigenic levels of those ultralarge vWF multimers required to cause platelet aggregation are considerably smaller than vWF antigen levels found in normal human plasma (1 unit/ml) (43, 44). In fact, they showed that antigenic levels of platelet-released vWF < 0.015 units/ml can cause massive platelet aggregation at relatively high shear stress (120 dynes/cm^2), in the presence of a small amount of ADP serving as a cofactor (43). The same group showed that 0.05 units/ml of EC-secreted vWF multimers is sufficient to cause massive platelet aggregation when platelets are sheared at 180 dynes/cm^2 (44).

With those numbers in mind, the data of Fig. 16 clearly indicate that platelet-released vWF multimers may be important in platelet/platelet adhesion in flowing systems and/or in thrombus consolidation due to bound vWF multimers on adjacent platelet membranes, especially at low and intermediate wall shear rates ($< 1,000 \text{ s}^{-1}$). This finding is particularly important because, while the role of vWF in inducing platelet-vessel wall and platelet/platelet

interaction has been reported as essential mostly at high shear rates (23, 45), these results and the recently reported experimental data by Badimon et al. (46) indicate that vWF may also modulate those effects at low wall shear rates.

CONCLUSIONS

When interpreting our data in the context of thrombus formation, it should be remembered that platelet-activating substances are known to act synergistically with each other. Therefore, subthreshold concentrations of one agent present with subthreshold concentrations of another agent may cause platelet activation. It has been found, for instance, that nanomolar quantities of ADP are sufficient to cause massive platelet aggregation, when combined with large or unusually large vWF multimers from plasma, platelets, or ECs (43).

Even in the presence of the anticoagulant heparin, thrombin appears to be the most important of the platelet-activating substances analyzed in this paper. The roles played by ADP and platelet-released vWF may be significant, especially at low shear rates and during the early stages of thrombus growth. The role of TxA_2 appears to be secondary, but for the reasons mentioned above, this low concentration of compound could stimulate platelets to respond with greater sensitivity to other activating agents. Furthermore, our results suggest that TxA_2 may become more important in the later stages of the thrombogenesis process, when the aggregates become larger and the concentrations of other agents such as ADP or thrombin diminish.

Standing vortices developing on both sides of individual thrombi and between nearby-growing thrombi are responsible for the observed rises in concentrations of platelet-activating agents within those regions, and give theoretical support to the experimentally-observed mechanisms of thrombus growth. Indeed, it has been reported that thrombi grow primarily from their downstream edges, and that massive platelet aggregation occurs in the spaces between nearby-growing thrombi. In other words, platelets accumulate preferentially in the regions of large platelet-activating agent concentrations and low fluid velocities. Finally, we observed that the average shear and tensile stresses, acting on the thrombi, increase with increasing blood flow rate, but are independent of thrombus size and only weakly dependent on thrombus geometry. In other words, embolization of such small protrusions may occur only at relatively high wall shear rate. In fact, this correlates well with the previous experimental observations from our laboratory (19, 24), that occasional embolization of the larger thrombi ($10\text{--}20 \mu\text{m}$ high) formed on collagen-coated glass occurred at wall shear

rates $\geq 1,500 \text{ s}^{-1}$. It is likely, however, that as the size of the aggregate increases, the embolizing stresses may become functions of both the wall shear rate and the thrombus size. In this context, it is probable that emboli forming in high flow rate vessels such as the arterioles, are much smaller than those developing in the venous system for instance. The latter ones, because of their large sizes, could be potentially more dangerous for they are prone to occlude small blood vessels distally.

APPENDIX A

The convection-diffusion equation describing the physical situation shown in Fig. 1 is given by

$$V_x \frac{\partial C_j}{\partial x} + V_y \frac{\partial C_j}{\partial y} = D_{j,e} \left[\frac{\partial^2 C_j}{\partial x^2} + \frac{\partial^2 C_j}{\partial y^2} \right] - k C_r, \quad (\text{A1})$$

where V_x and V_y represent the x and y components of the velocity vector; C_j is the concentration of the species of interest j ; $D_{j,e}$ is the effective diffusion coefficient of species j in whole blood; k is a bulk phase reaction rate constant; and C_r is the product of the reactant concentrations. For species E , $C_r = C_e$, while for species B , $C_r = C_b \times C_c$, where the subscripts refer to the species as defined in the Theory section.

Eq. A1 was solved with the following imposed boundary conditions: (a) on the thrombus surface:

$$C_a = 0; \quad D_{b,e} \frac{\partial C_b}{\partial n} = -D_{a,e} \frac{\partial C_a}{\partial n}; \quad D_{j,e} \frac{\partial C_j}{\partial n} = N_j \quad \text{for } j = e, g, \text{ or } h \quad (\text{A2})$$

(b) upstream from the thrombus ($x = x_0$) and on the top plate ($y = B$)

$$C_j = C_{j_0} \quad \text{for } j = a, c, h; \quad C_i = 0 \quad \text{for } i = b, e, g \quad (\text{A3})$$

(c) downstream from the thrombus ($x = x_e$)

$$\frac{\partial C_j}{\partial x} = 0 \quad \forall j, \quad (\text{A4})$$

where n is the direction normal to the boundary. For a given wall shear rate, the flux N_j is constant for ADP, TxA_2 , and vWF, and was calculated from experimental data, as explained in Appendix C. The flux of thrombin was estimated by first solving Eq. A1 for prothrombin, assuming a concentration of prothrombin equal to zero at the thrombus surface and then calculating the flux of prothrombin over the surface area of the object. That value, corrected for the difference in effective diffusion coefficients between the two compounds, was used as the thrombin flux. C_{j_0} represents the initial concentration of substance j in whole blood (see Table 1).

To solve Eq. A1, the equation of motion for an incompressible Newtonian fluid with constant physical properties (the Navier-Stokes equation), together with the continuity equation, had to be solved for the velocity field. Those equations, in vector notation, assuming steady state, are given by

$$\nabla \cdot \mathbf{V} = 0 \quad (\text{A5})$$

$$\rho \mathbf{V} \cdot \nabla \mathbf{V} = -\nabla P + \mu \nabla^2 \mathbf{V} + \mathbf{p}g \quad (\text{A6})$$

with the following boundary conditions:

(a) upstream ($x = x_0$):

$$V_y = 0; \quad V_x = V_{\max} \left[1 - \left(\frac{y}{B} \right)^2 \right] \quad (\text{parabolic profile}) \quad (\text{A7})$$

(b) along top and bottom plate ($y = \pm B$) and on the thrombus surface:

$$V_x = V_y = 0 \quad (\text{no slip}) \quad (\text{A8})$$

(c) downstream ($x = x_e$):

$$t_n = t_t = 0, \quad (\text{A9})$$

where V_x are V_y are respectively, the x and y components of the velocity vector \mathbf{V} ; V_{\max} is the maximum velocity at the center of the channel; P is the pressure; \mathbf{g} is the gravity field; ρ and μ are, respectively, the fluid density and viscosity; t_n and t_t are the normal and tangential components of the stress vector \mathbf{t} ; and ∇ is the Laplace operator. At the outflow boundary ($x = x_e$) the assumption of fully developed flow is made; the velocities are left free so that the boundary condition of zero stress in the normal and tangential directions is obtained.

Eq. A1–A9 were then dedimensionalized by introducing the following dimensionless quantities:

$$C_j^* = \frac{C_j D_{j,e}}{N_j B} \quad P^* = \frac{P}{\rho V_{\max}^2} \quad N^* = \frac{N_j}{Pe N_{j,\text{ref}}} \quad L^* = \frac{L}{B}$$

$$k^* = \frac{k B}{V_{\max}} \quad g^* = \frac{g B}{V_{\max}^2} \quad V^* = \frac{V}{V_{\max}},$$

L represents any length x , y , or n .

This yields, dropping the asterisks, the following system of weakly coupled partial differential equations (PDEs):

$$\nabla \cdot \mathbf{V} = 0 \quad (\text{A10})$$

$$\mathbf{V} \cdot \nabla \mathbf{V} = -\nabla P + \left(\frac{1}{Re} \right) \nabla^2 \mathbf{V} + \mathbf{g} \quad (\text{A11})$$

$$\mathbf{V} \cdot \nabla C_j = \left(\frac{1}{Pe} \right) (\nabla^2 C_j) - k C_r \quad (\text{A12})$$

with the following dimensionless boundary conditions:

(a) on the thrombus surface:

$$C_a = 0; \quad \frac{\partial C_b}{\partial n} = \frac{\partial C_a}{\partial n}; \quad \frac{\partial C_j}{\partial n} = 1.0 \quad (\text{A13})$$

for $j = e, g, \text{ or } h$

$$V_x = V_y = 0 \quad (\text{A14})$$

(b) at $x = x_0$ and $y = B$:

$$C_j = 0 \quad \text{for } j = b, e, \text{ or } g; \quad C_i = \frac{D_{i,e} C_{i_0}}{N_i B} \quad (\text{A15})$$

for $i = a, c, \text{ or } h$

(c) at $x = x_e$:

$$\frac{\partial C_j}{\partial x} = 0 \quad \forall j; \quad t_n = t_t = 0 \quad (\text{A16})$$

(d) at $x = x_0$:

$$V_y = 0; \quad V_x = 1 - y^2 \quad (\text{A17})$$

(e) at $y = \pm B$:

$$V_x = V_y = 0. \quad (\text{A18})$$

The dimensionless parameter Re is the Reynolds number ($\rho V_{\max} B/\mu$) which represents the ratio of inertial forces to viscous forces, and Pe is the Peclet number ($V_{\max} B/D_{\text{eff}}$) which is the ratio of mass transport by convection to mass transport by diffusion (47).

APPENDIX B

The system of weakly coupled PDEs and their boundary conditions, given by Eqs. A10–A18, was solved by a finite element routine for fluid flow, FIDAP (Fluid Dynamics International, Inc., Evanston, IL). A preprocessor, with automatic mesh refinement capability, was utilized to discretize the flow domain into a large number of elements. For a typical rectangular model thrombus 20 μm long, with the dimensions of the flow domain shown in Figs. 1 and 2, we used 361 isoparametric quadrilateral elements, each containing nine nodes, yielding a total of 1,549 nodal points. The Galerkin form of the Method of Weighted Residuals was the minimization technique chosen in our simulation. The velocity and concentration were approximated by a series of identical biquadratic interpolation functions, whereas discontinuous linear approximation functions were used for the pressure. The finite element method (FEM) was applied to a perturbed system of equations in which the continuity requirement, Eq. A10, was replaced by

$$\nabla \cdot \mathbf{V} = -\epsilon P, \quad (\text{B1})$$

where ϵ , the penalty parameter, was chosen as 10^{-6} . This approach has the advantage of eliminating the dependent variable P from the momentum equation without losing any significant accuracy, provided ϵ is small enough (48).

The application of the FEM to the momentum and convection-diffusion equations resulted in a set of nonlinear algebraic equations, represented in matrix (bold face) form as

$$\mathbf{L}(\mathbf{U})\mathbf{U} = \mathbf{F}, \quad (\text{B2})$$

where \mathbf{L} is the global system matrix, \mathbf{U} is the global vector of unknowns (velocities and concentrations), and \mathbf{F} is a vector which includes the effect of body forces and boundary conditions.

A combination of two different iterative algorithms were used to solve this system. First, the successive substitution (SS), or Picard iteration, scheme, given below, was applied:

$$\mathbf{L}(\mathbf{U}_i)\mathbf{U}_{i+1} = \mathbf{F}. \quad (\text{B3})$$

The Stokes solution for the velocity field and a null concentration vector served as the initial iterate \mathbf{U}_0 . The advantages of this method are its large radius of convergence and its insensitivity with respect to \mathbf{U}_0 . Because of its slow convergence rate, however, this technique was replaced, after three iterations, by the faster quasi-Newton (Broyden's update) (49) method of iteration, written as:

$$\mathbf{U}_{i+1} = \mathbf{U}_i - 0.8 \mathbf{D}_i; \quad \mathbf{D}_i = \mathbf{S}_i \mathbf{R}_i \quad (\text{B4})$$

$$\mathbf{S}_{i+1} = \mathbf{S}_i + \Delta \mathbf{S}_i \quad (\text{B5})$$

$$\Delta \mathbf{S}_i = \frac{(\lambda_{i+1} - \mathbf{S}_i \Gamma_{i+1}) \lambda_{i+1}^T}{\lambda_{i+1}^T \mathbf{S}_i \Gamma_{i+1}} \mathbf{S}_i, \quad (\text{B6})$$

where $\lambda_i = \mathbf{U}_i - \mathbf{U}_{i-1}$; $\Gamma_i = \mathbf{R}_i - \mathbf{R}_{i-1}$; \mathbf{R}_i is the residual force vector $\mathbf{R}(\mathbf{U}_i) = \mathbf{L}(\mathbf{U}_i)\mathbf{U}_i - \mathbf{F}$; and \mathbf{S}_i is the inverse of the Jacobian matrix of the system of equations $\mathbf{J}^{-1}(\mathbf{U}_i) = (\partial \mathbf{R}_i / \partial \mathbf{U}_i)^{-1}$. The initial \mathbf{S}_0 was calculated from $\mathbf{J}^{-1}(\mathbf{U}_0) = (\partial \mathbf{R}_0 / \partial \mathbf{U}_0)^{-1}$, where \mathbf{U}_0 is the solution vector of the last iteration by the SS method. This technique is more economical than the Newton-Raphson method, for instance, because it only updates \mathbf{S}_i at every iteration instead of recomputing it.

Iteration for the steady-state solution was terminated when the following two convergence criteria were satisfied simultaneously:

$$\frac{\|\mathbf{U}_i - \mathbf{U}_{i-1}\|}{\|\mathbf{U}_i\|} \leq 0.01 \quad (\text{B7})$$

$$\frac{\|\mathbf{R}_i - \mathbf{R}_{i-1}\|}{\|\mathbf{R}_0\|} \leq 0.01, \quad (\text{B8})$$

where the norm $\|\cdot\|$ is a root mean square norm summed over all nodes in the mesh.

The method adopted for solving the assembled matrix equation at each iteration step was the direct Gauss elimination with a skyline out-of-core storage mode initially developed by Hasbani and Engelman (50). Finally, a postprocessor was used to output the various solution variables in graphical form.

APPENDIX C

Flux

The wall fluxes of all platelet-activating substances, with the exception of thrombin, were estimated, as a function of wall shear rate, from a knowledge of their generation rates or amounts per platelet, and the growth rates or sizes of the model thrombi. Although values for those generation rates or amounts per platelet were obtained from other sources (51, 52) (see Table 1), the number of platelets constituting an average single thrombus at discrete times was measured in our laboratory at different wall shear rates by a technique previously reported (20). Next, by assuming an average platelet volume of 10 μm^3 , the average thrombus volume was also estimated. Both data sets were then curve-fitted with cubic polynomials using a least squares regression technique. The experimental data and the curves fitting those data are shown in Fig. 17.

The strategy used was to match the model thrombus volume to the measured average thrombus volume, and solve the resulting cubic polynomial for a feasible time root ($0 < t$ [seconds] < 150). The number of platelets per thrombus or the thrombus growth rate could then be estimated, at that specific time, from the polynomials (or their time derivatives) curve-fitting the data of Fig. 17. The details of the flux computations are shown below for the 20- μm -long hemispherical thrombus at 1,500 s^{-1} . Because the calculations for ADP and vWF are similar, only those for ADP are considered here.

ADP flux

80% of the ADP content of the dense granules in each platelet is assumed to be instantaneously released as the platelet attaches to the growing thrombus (51). The ADP flux is, therefore, essentially dependent upon the thrombus growth rate. From reference 51, a single platelet contains 3.0×10^{-17} moles of ADP inside its dense granules. The growth rate of the model thrombus is estimated from the experimental data as follows. The volume of a hemisphere, with a diameter of 20 μm , is $(2/3)(\pi)(10)^3$ or 2,094.4 μm^3 . The polynomial curve-fitting the data of Fig. 17 at 1,500 s^{-1} is then set equal to that value:

$$2,094.40 = -76.20 + 4.00(t) + 0.75(t)^2 - 2.11 \times 10^{-3}(t)^3,$$

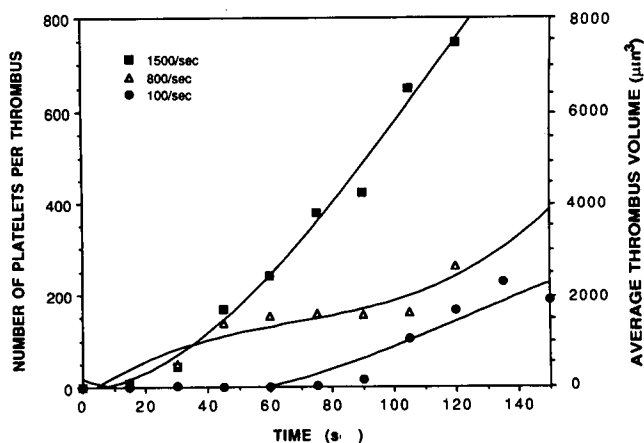


FIGURE 17 Number of platelets constituting an average single growing thrombus and average thrombus volume as a function of time and wall shear rate. The experimental data for the number of platelets were curve-fitted with the following cubic polynomials: $P_{1500} = -7.62 + 0.40t + 7.50 \times 10^{-2}t^2 - 2.11 \times 10^{-4}t^3$, $R^2 = 0.99$; $P_{800} = -21.80 + 4.71t - 5.22 \times 10^{-2}t^2 + 2.59 \times 10^{-4}t^3$, $R^2 = 0.90$; $P_{100} = 17.50 - 2.38t + 4.15 \times 10^{-2}t^2 - 1.10 \times 10^{-4}t^3$, $R^2 = 0.91$, where P and t represent, respectively, the number of platelets per thrombus and the time in seconds, and R^2 is the coefficient of determination, defined as $R^2 = (S_t - S_r)/S_t$, where S_t is the total sum of the squares around the mean, and S_r is the sum of the squares of the residuals around the regression line. The coefficients in the above polynomials have to be multiplied by 10 to obtain the polynomials curve-fitting the average thrombus volume data.

with t representing time in seconds. That equation is solved numerically for a feasible time root, and t , in this case, is found to be 55.5 s. The thrombus growth rate, at that specific time, may now be estimated by evaluating the time derivative of the corresponding polynomial representing the data of Fig. 17 at $1,500 \text{ s}^{-1}$, as following:

$$\left[\frac{d(plt)}{dt} \right]_{t=55.5} = 0.40 + 2(7.50 \times 10^{-2})(t) - 3(2.11 \times 10^{-4})(t)^2 = 6.80 \text{ plt/s}.$$

One may now calculate the ADP flux over a thrombus surface area of $(2)(\pi)(10)^2$ or $628.3 \mu\text{m}^2$, as:

$$\text{Flux (ADP)} = \frac{(6.80 \text{ plt/s})(3 \times 10^{-17} \text{ mol/plt})(0.80)}{628.3 \mu\text{m}^2} = 25.80 \times 10^{-20} \text{ mol}/\mu\text{m}^2 \text{ s}.$$

TxA₂ flux

Because TxA₂ is generated enzymatically within the platelet, its flux depends primarily on the number of platelets composing the thrombus, rather than on the thrombus growth rate. It is also assumed that its intracellular precursor, arachidonic acid, is present in excess, therefore not limiting TxA₂ metabolism. Furthermore, because the internal diffusion of TxA₂ from the thrombus core to the outside fluid was not taken into account when estimating the wall fluxes of that compound, the calculated concentration profiles represent upper bounds on those observed experimentally. From the measurements of reference 52 and calculations similar to those of reference 15, TxA₂ generation rate per platelet is estimated to be $0.95 \times 10^{-20} \text{ mol/s}$. The model thrombus size

at $t = 55.5 \text{ s}$ is computed by evaluating the polynomial curve-fitting the data of Fig. 17 at $1,500 \text{ s}^{-1}$, as following:

$$[\text{No. platelets}]_{t=55.5} = -7.62 + 0.40(t) + 7.50 \times 10^{-2}(t)^2 - 2.11 \times 10^{-4}(t)^3 = 209.40 \text{ plt}.$$

The TxA₂ flux may now be calculated as:

$$\text{Flux (TxA}_2) = \frac{(209.40 \text{ plt})(0.95 \times 10^{-20} \text{ mol/plt s})}{628.3 \mu\text{m}^2} = 3.20 \times 10^{-21} \text{ mol}/\mu\text{m}^2 \text{ s}.$$

Table 3, for circular model thrombi, and Table 4, for rectangular ones, summarize all experimentally derived data, including platelet-activating agent fluxes, the sizes and growth rates of model thrombi, and the time roots as a function of wall shear rate and model thrombus size.

Reaction rate constants

The detailed calculations of the chemical reaction rate constant for the nonenzymatic hydrolysis of TxA₂ to TxB₂ in aqueous medium are given in reference 15. The value used is given in Table 1.

Inactivation of thrombin by AT III

Thrombin is inactivated, in the bulk phase, by the circulating AT III, assumed to be present in excess around the thrombus ($[\text{AT III}] \gg [\text{T}]$, where $[\text{AT III}]$ is the AT III molar concentration and $[\text{T}]$ is the thrombin molar concentration). The whole blood concentration of AT III is $\sim 2.844 \mu\text{M}$, assuming a plasma concentration of 29 mg/dl (9) and an average hematocrit of 39.2%. The observed second order rate constant, k''_{obs} , was measured in reference 53 to be $4.25 \times 10^5 \text{ M}^{-1} \text{ min}^{-1}$, with a reaction rate equation of the form: $-d[\text{T}]/dt = k''_{\text{obs}}[\text{AT III}][\text{T}]$. An observed pseudo-first order reaction rate constant, k'_{obs} , may now be estimated according to $k'_{\text{obs}} = k''_{\text{obs}}[\text{AT III}]$, and in the present case, turns out to be 0.0201 s^{-1} .

Inactivation of thrombin by AT III in presence of heparin

Inhibition of thrombin by AT III is greatly accelerated in presence of heparin. To fully investigate the inhibitory effect of heparin, we performed calculations with two different heparin concentrations, the experimentally used concentration and the concentration for maximum rate of inhibition, as determined by the data in reference 25. Heparin, with a specific activity of 300 USP U/mg, is used in concentration of 10 U/ml of blood in our experiments, which corresponds to a whole blood concentration of $2.0833 \mu\text{M}$. From Fig. 1 in reference 25, the observed second order rate constant k''_{obs} is $\sim 0.25 \times 10^9 \text{ M}^{-1} \text{ min}^{-1}$ at that heparin concentration. The observed pseudo first order rate constant, k'_{obs} , may be estimated as reported above and is found to be 11.85 s^{-1} . From the same figure in reference 25, the maximum rate of inhibition for that reaction occurs at $[\text{heparin}] = 9.0 \times 10^{-8} \text{ M}$, and with $k''_{\text{obs}} = 2.68 \times 10^9 \text{ M}^{-1} \text{ min}^{-1}$. k'_{obs} is 127.0 s^{-1} in this case. All reaction rate constants are summarized in Table 1.

Physical Parameters

All physical parameters were estimated as constant average quantities, for a given wall shear rate, in our model. Assuming a homogeneous fluid, most parameters were calculated on the basis of an average shear rate $\langle \dot{\gamma} \rangle$ across the channel, which, for a parabolic velocity profile, is given

by

$$\langle \dot{\gamma} \rangle = \frac{1}{B} \int_0^B \dot{\gamma}(x) dx = \frac{\dot{\gamma}_{\text{wall}}}{2}. \quad (\text{C1})$$

Those assumptions are justified, for the present model, by the facts that the crowding of RBCs in the center of the vessel (rouleaux formation), leading to a large plasmatic layer near the wall surface, and thereby to a nonuniform cell distribution across the channel, occurs predominantly in vessels of very small diameter. Also, the non-Newtonian behavior of blood, another consequence of the nonuniform RBC distribution, which can lead to a nonparabolic velocity profile, is important primarily at very low shear rates ($<100 \text{ s}^{-1}$) (54).

Because it has been shown (55) that, in vessels with diameters smaller than $\sim 500 \mu\text{m}$, the average hematocrit in the tube, h_t , is less than the hematocrit of the entering fluid, h_e (chosen arbitrarily as 40% here), a phenomenon referred to as the *Fåhræus effect*, the magnitude of that effect was estimated theoretically by the authors for the present model. Based on Lih's model derived for a tube with a stepwise RBC distribution (54), and using, as a first approximation, Einstein's model for the hematocrit-dependency of viscosity (54), h_t was calculated to be 39.2%, indicating that the Fåhræus effect is relatively weak in our model. That value was used, however, in all subsequent calculations involving hematocrit.

Because blood viscosity is known to be a weakly decreasing function of shear rate ($\dot{\gamma} > 100 \text{ s}^{-1}$) (56), an average viscosity was estimated at each shear rate (see Table 2), using an equation derived by Quemada, that represents the rheological properties of blood and related red cell suspensions over a wide range of conditions (55).

Because the problem treated is essentially an isothermal one, with a constant temperature of 37°C , the density of blood was considered constant at 1.1064 g/cm^3 in all calculations.

When RBCs are present in a nonuniform velocity field, such as exists in parallel plate flow, the cells rotate, entraining the small fluid layers surrounding the cells to rotate also. Those local secondary flows greatly augment the effective diffusivities of cells and large molecular weight species, particularly vWF multimers and thrombin, when compared to Brownian diffusion alone. Keller (11) has developed a model which gives the effective diffusion coefficient, D_e , as:

$$D_e = D_b + D_i, \quad (\text{C2})$$

where D_b is the Brownian molecular diffusion coefficient (see Table 1), and D_i is the rotation-induced diffusion coefficient (see Table 2), given by:

$$D_i = 0.18\delta^2\dot{\gamma}_{\text{wall}}, \quad (\text{C3})$$

where δ is the equivalent RBC radius.

Because the thrombogenesis process occurs predominantly near the wall surface, where RBC concentration is low, it is postulated that the enhanced diffusivity is due primarily to RBC rotation rather than to interparticle collision, which may be the prevailing mechanism in the bulk. For the same reason, the wall shear rate $\dot{\gamma}_{\text{wall}}$, rather than the average shear rate $\langle \dot{\gamma} \rangle$ is used in Eq. C3. The parameters for the platelet-activating agents and the chemical reactions, and the shear rate-dependent physical parameters are summarized in Tables 1 and 2, respectively.

Received for publication 29 December 1988 and in final form 8 June 1989.

REFERENCES

1. Bounameaux, Y. 1959. L'accrolement des plaquettes aux fibres sous endothéliales. *CR Seances Soc. Biol.* 153:865-867.
2. Sixma, J. J., and J. Wester. 1977. The hemostatic plug. *Semin. Hematol.* 14:265-299.
3. Hirsh, J., and E. A. Brain. 1983. Hemostasis and Thrombosis: A Conceptual Approach. Churchill Livingstone, New York. 164 pp.
4. Turitto, V. T., and H. R. Baumgartner. 1982. Platelet-surface interactions. In *Hemostasis and Thrombosis: Basic Principles and Clinical Practice*. R. W. Colman, J. Hirsh, V.J. Marder, and E. W. Salzman, editors. J. B. Lippincott Company, Philadelphia. 364-379.
5. Anderson, J. M., and K. Kottke-Marchant. 1985. Platelet interactions with biomaterials and artificial devices. *CRC Crit. Rev. Biocompat.* 1:111-204.
6. Sussman, I. I. 1985. The role of platelets in atherogenesis/atherosclerosis. In *The Platelets: Physiology and Pharmacology*. G. L. Longenecker, editor. Academic Press, Orlando. 383-405.
7. Kinlough-Rathbone, R. L., and J. F. Mustard. 1986. Synergism of agonists. In *Platelet Responses and Metabolism*. H. Holmsen, editor. CRC Press, Boca Raton. 1:193-207.
8. Baumgartner, H. R., and R. Muggli. 1976. In *Platelets in Biology and Pathology*. J. R. Gordon, editor. Biomedical Press, North Holland. 23-60.
9. Report of the National Heart, Lung, and Blood Institute Working Group. 1985. Concepts of thrombus formation, dissolution, and antithrombotic therapy. In *Guidelines For Blood-Material Interactions* (NIH publication no. 85-2185). 19-63.
10. Eckstein, E. C. 1982. Rheophoresis—A broader concept of platelet dispersivity. *Biorheology.* 19:717-724.
11. Keller, K. H. 1971. Effect of fluid shear on mass transport in flowing blood. *Fed. Proc.* 30:1591-1599.
12. Wang, N-H. L., and K. H. Keller. 1985. Augmented transport of extracellular solutes in concentrated erythrocyte suspensions in couette flow. *J. of Colloid Interface Sci.* 103:210-225.
13. Morton, L. F., and M. J. Barnes. 1982. Collagen polymorphism in the normal and diseased blood vessel wall: investigations of collagen types I, III, and V. *Atherosclerosis.* 42:41-51.
14. Butruille, Y. A., E. F. Leonard, and R. S. Litwak. 1975. Platelet-platelet interactions and non-adhesive encounters on biomaterials. *Trans. Am. Soc. Artif. Intern. Organs.* 21:609-614.
15. Hubbell, J. A., and L. V. McIntire. 1986. Platelet active concentration profiles near growing thrombi—A mathematical consideration. *Biophys. J.* 50:937-945.
16. Karino, T., and H. L. Goldsmith. 1979a. Aggregation of human platelets in an annular vortex distal to a tubular expansion. *Microvasc. Res.* 17:238-262.
17. Karino, T., and H. L. Goldsmith. 1979b. Adhesion of human platelets to collagen on the walls distal to a tubular expansion. *Microvasc. Res.* 17:238-262.
18. Niyibizi, C., P. P. Fietzek, and M. van der Rest. 1984. Human placenta type V collagens: evidence for the existence of an $\alpha 1(\text{V})\alpha 2(\text{V})\alpha 3(\text{V})$ collagen molecule. *J. Biol. Chem.* 259:14170-14174.
19. Folie, B., and L. V. McIntire. 1988. Effects of a novel antiplatelet agent in mural thrombogenesis on collagen-coated glass. *Blood.* 72:1393-1400.

20. Hubbell, J. A., and L. V. McIntire. 1986. Technique for visualization and analysis of mural thrombogenesis. *Rev. Sci. Instrum.* 57:892-897.
21. Gelman, R. A., D. C. Poppke, and K. A. Piez. 1979. Collagen fibril formation in vitro, the role of the nonhelical terminal regions. *J. Biol. Chem.* 254:11741-11745.
22. Barnes, M. J. 1982. The collagen-platelet interaction. *In* Collagen in Health and Disease. J. B. Weiss and M. I. V. Jayson, editors. Churchill Livingstone, Inc., New York. 179-197.
23. Houdijk, W. P. M., K. S. Sakariassen, P. F. E. M. Nievelein, and J. J. Sixma. 1985. Role of factor VIII-von Willebrand factor and fibronectin in the interaction of platelets in flowing blood with monometric and fibrillar human collagen types I and III. *J. Clin. Invest.* 75:531-540.
24. Hubbell, J. A., and L. V. McIntire. 1986. Visualization and analysis of mural thrombogenesis on collagen, polyurethane, and nylon. *Biomaterials.* 7:354-363.
25. Griffith, M. J. 1982. Kinetics of the heparin-enhanced antithrombin III/thrombin reaction—Evidence for a template model for the mechanism of action of heparin. *The J. Biol. Chem.* 257:7360-7365.
26. Hammarstrom, S., J. A. Lindgren, and P. Ross. 1979. Biosyntheses of prostaglandins and thromboxanes. *In* Chemistry, Biochemistry and Pharmacological Activity of Prostanoids. S. M. Roberts and F. Scheinmann, editors. Pergamon Press, Oxford. 221-232.
27. Rozenberg, M. C., and H. Holmsen. 1968. Adenine nucleotide metabolism of blood platelets. IV. Platelet aggregation response to exogenous ATP and ADP. *Biochim. Biophys. Acta.* 157:280-288.
28. Williams, W. J. 1983. Life-span of plasma coagulation factors. *In* Hematology. W. J. Williams, E. Beutler, A. J. Ersley, and M. A. Lichtman, editors. McGraw-Hill, Inc., New York. 1230-1237.
29. Schlichting, H. 1979. Boundary-layer Theory. McGraw-Hill, Inc., New York. 2 pp.
30. Turitto, V. T., H. J. Weiss, H. R. Baumgartner, L. Badimon, and V. Fuster. 1987. Cells and Aggregates at Surfaces. *In* Blood in Contact with Natural and Artificial Surfaces. E. F. Leonard, V. T. Turitto, and L. Vroman, editors. Ann. N. Y. Acad. Sci. 516:453-467.
31. Dennis, S. C. R., and G. Z. Chang. 1970. Numerical solutions for steady flow past a cylinder at Reynolds number up to 100. *J. Fluid Mech.* 42:471-489.
32. Kiya, M., and M. Arie. 1975. Viscous shear flow past small bluff bodies attached to a plane wall. *J. Fluid Mech.* 69:803-823.
33. Hyman, M. A. 1972. Shear flow over a protrusion from a plane wall. *J. Biomech.* 5:45-48.
34. Mills, R. D. 1968. Numerical solutions of viscous flow through a pipe orifice at low Reynolds numbers. *J. Mech. Engrg. Sci.* 10:133-140.
35. Basmadjian, D. 1984. The hemodynamic forces acting on thrombi, from incipient attachment of single cells to maturity and embolization. *J. Biomech.* 17:287-298.
36. Adams, G. A., S. J. Brown, L. V. McIntire, S. G. Eskin, and R. R. Martin. 1983. Kinetics of platelet adhesion and thrombus growth. *Blood.* 62:69-74.
37. Weiss, H. J. 1982. Platelets: Pathophysiology and Antiplatelet Drug Therapy. Alan R. Liss Inc., New York. 165 pp.
38. Jones, R. L., N. H. Wilson, and C. G. Marr. 1979. Thromboxane-like activity of prostanoids with aromatic substituents at C16 and C17. *In* Chemistry, Biochemistry and Pharmacological Activity of Prostanoids. S. M. Roberts and F. Scheinmann, editors. Pergamon Press, Oxford. 210-220.
39. Baumgartner, H. R. 1979. Effects of acetylsalicylic acid, sulfinpyrazone and dipyridamole on platelet adhesion and aggregation in flowing native and anticoagulated blood. *Haemostasis.* 8:340.
40. Heras, M., J. H. Chesebro, W. J. Penny, L. Badimon, and V. Fuster. 1988. Recombinant hirudin documents the central role of thrombin during arterial angioplasty. *Supplement II Circulation.* 78:311.
41. Jang, I-K., A. A. Ziskind, H. K. Gold, R. C. Leinbach, J. T. Fallon, and D. Collen. 1988. Prevention of arterial platelet occlusion by selective thrombin inhibition. *Supplement II Circulation.* 78:311.
42. Schneider, P. A., S. R. Hanson, and L. A. Harker. 1988. Permanent interruption of thrombus formation on carotid endarterectomy sites by short-term therapy with a synthetic antithrombin. *Supplement II Circulation.* 78:311.
43. Moake, J. L., N. A. Turner, N. A. Stathopoulos, L. H. Nolasco, and J. D. Hellums. 1988. Shear-induced platelet aggregation can be mediated by vWF released from platelets, as well as by exogenous large or unusually large vWF multimers, requires adenosine diphosphate, and is resistant to aspirin. *Blood.* 71:1366-1374.
44. Moake, J. L., N. A. Turner, N. A. Stathopoulos, L. H. Nolasco, and J. D. Hellums. 1986. Involvement of large plasma von Willebrand Factor (vWF) multimers and unusually large vWF forms derived from endothelial cells in shear stress-induced platelet aggregation. *J. Clin. Invest.* 78:1456-1461.
45. Baumgartner, H. R., T. B. Tshchopp, and D. Meyer. 1980. Shear rate dependent inhibition of platelet adhesion and aggregation on collagenous surfaces by antibodies to human factor VIII/von Willebrand factor. *Br. J. Haematol.* 44:127-139.
46. Badimon, L., J. J. Badimon, V. Turitto, and V. Fuster. 1988. Von Willebrand factor mediates platelet vessel wall interaction at low shear rates. *Supplement II Circulation.* 78:254.
47. Bird, R. B., W. E. Stewart, and E. N. Lightfoot. 1960. Transport Phenomena. John Wiley & Sons Inc., New York. 780 pp.
48. Bercovier, M. 1976. These de Doctorat d'Etat. Rouen.
49. Broyden, C. G. 1965. A class of methods for solving nonlinear simultaneous equations. *Math. Comp.* 19:577-593.
50. Hasbani, I., and M. Engelman. 1979. Out of core solution of linear equations with non-symmetric coefficient matrix. *Comp. and Fluids.* 7:13-31.
51. Adams, G. A., and I. A. Feuerstein. 1983. Maximum fluid concentrations of materials released from platelets at a surface. *Am. J. Physiol.* 244:H109-H114.
52. De Caterina, R., D. Giannessi, P. Gazzetti, and W. Bernini. 1984. Thromboxane-B₂ generation during ex-vivo platelet aggregation. *J. Nucl. Med. All. Sci.* 28:185-196.
53. Rosenberg, R. D. 1982. Heparin-Antithrombin system, *In* Hemostasis and Thrombosis: Basic Principles and Clinical Practice. R. W. Colman, J. Hirsh, V. J. Marder, and E. W. Salzman, editors. J. B. Lippincott Company, Philadelphia. 962-985.
54. Lih, M. M-S. 1975. Transport Phenomena in Medicine and Biology. John Wiley & Sons Inc., New York. 531 pp.
55. Cokelet, G. R. 1987. The rheology and tube flow of blood. *In* Handbook of Bioengineering. R. Skalak and S. Chien, editors. McGraw-Hill, Inc., New York. 14.1-14.17.
56. Karino, T., and H. L. Goldsmith. 1985. Rheological factors in thrombosis and haemostasis (2nd edition). *In* Haemostasis and Thrombosis. A. L. Bloom and D. P. Thomas, editors. Churchill Livingstone, Inc., London. 1-28.